

**Event Selection and Trigger Studies  
for an Analysis of the  
Forward – Backward Asymmetry  
of Muon Pairs  
at the Belle Experiment**

**Ereignisselektion und Triggerstudien für eine Analyse  
der Vorwärts – Rückwärts – Asymmetrie von  
Myonenpaaren beim Belle – Experiment**

**vorgelegt von  
Kim Susan Petersen  
geboren am  
06.10.1988**

**Master – Arbeit im Studiengang Physik  
Universität Hamburg**

**2013**

1. Gutachterin: Prof. Dr. Caren Hagner
2. Gutachter: Dr. Carsten Niebuhr



# Event Selection and Trigger Studies for an Analysis of the Forward – Backward Asymmetry of Muon Pairs at the Belle Experiment

## Abstract

This thesis is a first step towards an analysis of the muon pair forward – backward charge asymmetry  $A_{FB}$  of muon pairs with Belle data.  $A_{FB}$  is related to the weak mixing angle  $\sin(\theta_W)^2$  and is of the order  $10^{-3}$  at  $\sqrt{s} \approx 10$  GeV. A Monte Carlo (MC) based event selection and a both MC and data based trigger investigation are presented here. Results: An unphysical efficiency drop of subtrigger bits depending on input from the Central Drift Chamber (CDD) was discovered in the trigger simulation for the signal MC. One of the three apparently unaffected experiments was used to determine the polar angle – dependent trigger efficiency of the most important trigger bit, the CDC and  $K_L$ /muon detector dependent `k1m_opn` trigger – both from signal MC and experimental data. Therefore, the orthogonal calorimeter dependent `hie` trigger was used. A comparison of the efficiencies determined from data and MC shows clearly that one should not rely on the trigger simulation of the signal MC for further analyses, but use the data based `k1m_opn` efficiency to correct the signal MC with.

## Ereignisselektion und Triggerstudien für eine Analyse der Vorwärts – Rückwärts – Asymmetrie von Myonpaaren beim Belle – Experiment

### Zusammenfassung

Diese Arbeit ist ein erster Schritt in Richtung einer Analyse der Vorwärts – Rückwärts – Ladungsasymmetrie  $A_{FB}$  von Myonenpaaren mit Belle – Daten.  $A_{FB}$  ist mit dem schwachen Mischungswinkel  $\sin(\theta_W)^2$  verwandt und liegt in der Größenordnung  $10^{-3}$  für  $\sqrt{s} \approx 10$  GeV. Eine Monte Carlo (MC) basierte Ereignisselektion und eine sowohl MC – als auch datenbasierte Triggeruntersuchung werden hier präsentiert. Ergebnisse: Ein unphysikalischer Effizienzeinbruch der Subtriggerbits, die von der Zentralen Driftkammer (CDC) abhängig sind, wurde in der Triggersimulation des Signal – MCs entdeckt. Eins der drei anscheinend nicht betroffenen Experimente wurde benutzt um die polarwinkelabhängige Triggereffizienz des wichtigsten Triggerbits, des von der CDC und dem  $K_L$ /Myon – Detektor abhängigen `k1m_opn` Triggers, zu bestimmen – sowohl aus dem MC also auch mit experimentellen Daten. Dazu wurde der orthogonale, kalorimeterabhängige `hie` Trigger verwendet. Ein Vergleich der aus Daten und MC bestimmten Effizienzen zeigt eindeutig, dass man weitere Analysen nicht auf die Triggersimulation des Signal – MCs stützen, sondern die datenbasierte `k1m_opn` Effizienz benutzen sollte um das Signal – MC damit zu korrigieren.



# Contents

<b>1</b>	<b>Introduction</b>	<b>1</b>
<b>2</b>	<b>Theory</b>	<b>2</b>
2.1	Electroweak Interactions in the Standard Model and the Effective Weak Mixing Angle . . . . .	3
2.2	The Forward–Backward Asymmetry $A_{\text{FB}}$ . . . . .	5
2.3	Radiative corrections . . . . .	7
<b>3</b>	<b>The Belle Experiment</b>	<b>8</b>
3.1	The KEKB Accelerator . . . . .	8
3.2	The Belle Detector . . . . .	9
3.3	The Belle Trigger System . . . . .	12
3.4	Data Handling and Monte–Carlo Simulation . . . . .	14
<b>4</b>	<b>Analysis</b>	<b>17</b>
4.1	Background Events . . . . .	17
4.2	Event Selection . . . . .	19
4.3	Determination of L1 Trigger Efficiencies . . . . .	30
4.3.1	Monte–Carlo based Trigger Efficiencies . . . . .	30
4.3.2	Trigger Efficiency from Orthogonal Triggers . . . . .	44
<b>5</b>	<b>Conclusion</b>	<b>51</b>
<b>A</b>	<b>The Fast Track Finder Fzisan</b>	<b>53</b>
	List of Tables	54
	List of Figures	54
	Bibliography	56
	Formal and Personal Issues	60



# Chapter 1

## Introduction

The forward–backward charge asymmetry  $A_{FB}$  of muon pairs produced in electron positron annihilation has been studied by many experiments. It is connected to the weak mixing angle, which determines the relative contributions of electromagnetic and weak forces, and depends on the center–of–mass energy. The center–of–mass energy at the Belle Experiment, which was located at the asymmetric  $e^+e^-$  collider KEKB in Tsukuba (Japan), was about 10.58 GeV. KEKB reached an integrated luminosity of more than  $1 \text{ ab}^{-1}$ . This corresponds to roughly one billion muon pairs. Belle’s successor, Belle II at SuperKEKB, is going to benefit from an instantaneous luminosity forty times as high with respect to that at KEKB.

The main challenge of an  $A_{FB}$  analysis with Belle data is that  $A_{FB}$  is very small – at the order of  $10^{-3}$  – at Belle energies. In order to be competitive with other experiments and able to probe New Physics (like additional loops or coupling strengths deviating from Standard Model predictions), the measurement must be of a precision of about  $10^{-5}$ . While Belle is limited by its statistics, this goal should be achievable at Belle II.

This thesis is a first step towards an  $A_{FB}$  analysis with Belle data. The theoretical background is presented in chapter 2, followed by a detailed introduction of KEKB and the Belle Detector in chapter 3. The analysis part, which can be found in chapter 4, is divided into two sections. Firstly, the selection criteria used to select clean  $e^+e^- \rightarrow \mu^+\mu^-$  events are presented. Here, the main goals were the elimination of photons by cuts on the invariant mass of the two muons and on the photon energy, as well as the suppression of Bhabha events and other background channels. Secondly, based on this event selection, a Level 1 trigger investigation was carried out. While in many of the B–physics analyses carried out with Belle data the trigger efficiency can be assumed to be 100%, this is not possible for a high–precision muon pair analysis. Thus, the trigger efficiency has to be reevaluated and described as function of the polar angle  $\theta$ , such that it can be corrected for when fitting the angular distribution of the muon pair in order to determine  $A_{FB}$ . Not its absolute value but the angular shape of  $\epsilon_{L1}$  is important here, as well as its uncertainties. The results of the event selection and trigger investigation are summed up and discussed briefly in chapter 5.

## Chapter 2

# Theory

In the Standard Model (SM) of particle physics all known interactions between elementary particles – except for gravity – are described. The elementary particles are categorized as leptons and quarks, respectively, which are both represented by fermion fields (spin 1/2). The mathematical description of the SM is based on the  $SU(3)_C \otimes SU(2)_L \otimes U(1)_Y$  gauge group, where  $C$  stands for color charge,  $L$  implies that  $SU(2)_L$  acts on left-handed fermions only, and  $Y$  denotes the electroweak hypercharge. The existence of the gauge bosons ( $\gamma$ ,  $W^\pm$ ,  $Z^0$  and gluons, all spin 1) follows from the principle of gauge invariance. In addition, the so-called Higgs mechanism is responsible for fermion and boson mass generation and implies the existence of another particle, the Higgs boson (spin 0). More details on the Higgs mechanism can be found in [1, 2, 3]. Figure 2.1 shows an overview of all SM bosons and fermions and also indicates their interactions with each other.

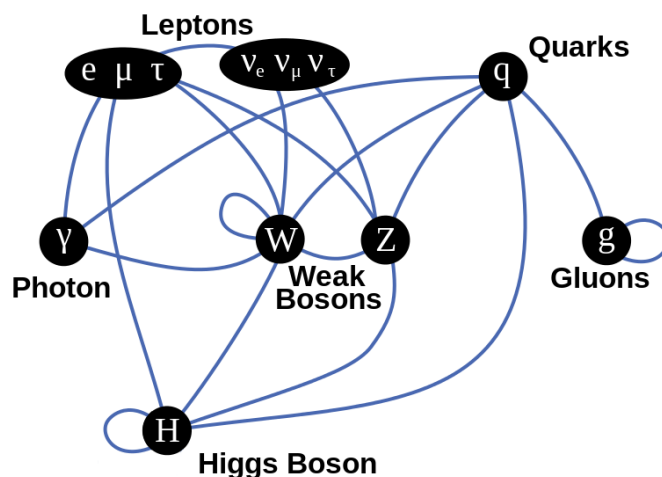


**Figure 2.1:** Elementary particles (black circles) and their interactions with each other (blue lines) [4].

In this chapter, more light will be shed onto the  $SU(2)_L \otimes U(1)_Y$  symmetry group. More specifically, the weak mixing angle, as well as its connection to the forward–backward charge asymmetry  $A_{FB}$  in muon–pair production, will be introduced, followed by a short discussion of radiative corrections.

## 2.1 Electroweak Interactions in the Standard Model and the Effective Weak Mixing Angle

Within the SM, weak and electromagnetic interactions are described by the  $SU(2)_L \otimes U(1)_Y$  symmetry group, as proposed by Glashow [5], Salam [6] and Weinberg [7]. The  $SU(2)_L$  symmetry couples to the third component of the weak isospin ( $I_3$ ) of left–handed fermions.  $I_3$  and the hypercharge  $Y$ , on which  $U(1)_Y$  acts, are connected with the electric charge  $Q$  via the Gell–Mann–Nishijima [8, 9] relation:

$$Q = I_3 + Y/2. \quad (2.1)$$

The three  $SU(2)_L$  and one  $U(1)_Y$  induced gauge bosons are represented by the massless fields  $W_\mu^{1,2,3}$  and  $B_\mu$ . By spontaneous symmetry breaking, the physical fields of the charged and neutral vector bosons  $W_\mu^\pm$  and  $Z_\mu$ , as well as the photon field  $A_\mu$ , are created.  $W_\mu^\pm$  are superpositions of the  $W_\mu^{1,2}$  fields:

$$W_\mu^\pm = \frac{1}{\sqrt{2}}(W_\mu^1 \pm iW_\mu^2), \quad (2.2)$$

whereas  $Z_\mu$  and  $A_\mu$  are connected to  $B_\mu$  and  $W_\mu^3$  via a rotation matrix:

$$\begin{pmatrix} Z_\mu \\ A_\mu \end{pmatrix} = \begin{pmatrix} \cos \theta_W & \sin \theta_W \\ -\sin \theta_W & \cos \theta_W \end{pmatrix} \begin{pmatrix} W_\mu^3 \\ B_\mu \end{pmatrix}, \quad (2.3)$$

with  $\theta_W$  (usually stated as  $\sin^2 \theta_W$ ) being the weak mixing angle, also known as the Weinberg angle. The weak couplings  $g$  and  $g'$  are connected with each other and the elementary charge  $e$  via the weak mixing angle as well:

$$e = g' \cos \theta_W = g \sin \theta_W. \quad (2.4)$$

Since the couplings between the Higgs field and the fields of the gauge bosons can be interpreted as mass terms, the masses of the gauge bosons can be written in terms of these couplings and the vacuum expectation value  $v$  of the Higgs field:

$$M_\gamma = 0, \quad M_W = \frac{v}{2} g' \text{ and } M_Z = \frac{v}{2} \sqrt{g'^2 + g^2}. \quad (2.5)$$

Therefore, the weak mixing angle can also be expressed in terms of the  $W$  and  $Z$  boson masses:

$$\sin^2 \theta_W = 1 - \frac{M_W^2}{M_Z^2}. \quad (2.6)$$

On tree-level, the electroweak mixing angle can as well be expressed by the ratio of the (axial-) vector fermion couplings:

$$\frac{g_{V,\text{tree}}^f}{g_{A,\text{tree}}^f} = 1 - 4|Q_f| \sin^2\theta_W, \quad (2.7)$$

with  $Q_f$  being the fermion charge, the couplings being defined as

$$g_{A,\text{tree}}^f = I_3^f, \quad (2.8)$$

$$g_{V,\text{tree}}^f = I_3^f - 2Q_f \sin^2\theta_W, \quad (2.9)$$

and using that  $Q_f \in \{-1, 0\}$  and  $Y = -1$  for left-handed fermions.

Higher order corrections due to additional quantum loop diagrams have to be taken into account though. To that purpose, the (energy scale dependent) form factors  $\rho^f(Q)$  and  $\kappa^f(Q)$  are introduced [10] (see chapter 2.3 for more information on radiative corrections). The *effective* weak mixing angle and the *effective* fermion couplings are then written as:

$$g_A^f = \sqrt{\rho^f} I_3^f, \quad (2.10)$$

$$g_V^f = \sqrt{\rho^f} \left( I_3^f - 2Q_f \sin^2\theta_{W(\text{eff})}^f \right), \quad (2.11)$$

$$\sin^2\theta_{W(\text{eff})}^f = \kappa^f \sin^2\theta_W, \quad (2.12)$$

leading to the more general expression:

$$\frac{g_V^f}{g_A^f} = 1 - 4|Q_f| \sin^2\theta_{W(\text{eff})}^f. \quad (2.13)$$

Not only does this mean that the weak mixing angle is an energy-dependent quantity, but most notably that precise measurements of its value are sensitive to New Physics, which would enter in the quantum loop corrections.

Up to today, various  $\sin^2\theta_{W(\text{eff})}$  measurements at different energy scales  $Q$  and for different processes have been performed. A selection of them is marked in Figure 2.2, which shows the theoretical prediction of the weak mixing angle's energy-dependence. Notable is here the NuTeV experiment ( $Q \approx 4 \text{ GeV}$ ), in which  $\sin^2\theta_{W(\text{eff})}$  has been extracted from deep inelastic neutrino nucleon scattering by measuring a ratio of charged current and neutral current processes [11]. There is a  $3\sigma$  tension between the measured and the predicted SM value.

With the Belle and NuTeV experiments being not too far apart on the energy scale, this is one of the reasons a Belle measurement of the weak mixing angle is of particular interest; especially keeping in mind that the process  $e^+e^- \rightarrow \mu^+\mu^-$ , used in the corresponding Belle analysis, is much cleaner (no nuclear effects have to be considered).

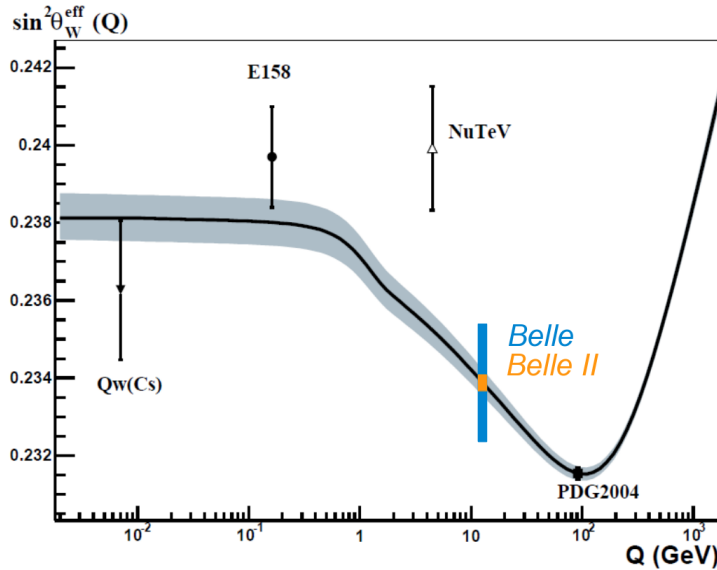


**Figure 2.2:** Expected Belle sensitivity and theoretically predicted  $\sin^2\theta_{W(\text{eff})}$  (black line) as a function of the momentum transfer  $Q$ , and its estimated theoretical uncertainty (gray band). Marked are the results of several experiments, namely a precision measurement of parity non-conservation in Cesium [12], the E158 experiment ( $e^+e^- \rightarrow e^+e^-$  Møller scattering) [13] and the NuTeV experiment [11], such as the 2004 PDG value (LEP/SLAC [14]). The blue (orange) line indicates the expected statistical error of the Belle (Belle II) measurement; the vertical position was chosen arbitrarily. Figure adapted from [13].

An early measurement of the quantity has been performed, for example, by the JADE Collaboration at PETRA for center-of-mass energies between 12 GeV and 46 GeV [15]. The precision of their result,  $\sin^2\theta_W = 0.18_{-0.02}^{+0.03} \pm 0.01$ , is no longer competitive to that of newer measurements though. The most precise value for the weak mixing angle comes from a combined SLAC<sup>1</sup>/LEP<sup>2</sup> measurement at the Z pole. Their average is given as  $\sin^2\theta_{W(\text{eff})}^{\text{leptons}} = 0.23153 \pm 0.00016$ ; the individual measurements differ by roughly three standard deviations though [14]. The ATLAS [16], CDF [17], CMS [18] and D0 [19] experiments have performed measurements at the Z pole as well.

## 2.2 The Forward–Backward Asymmetry $A_{FB}$

In the electroweak process  $e^+e^- \rightarrow \mu^+\mu^-$  the (effective) weak mixing angle can be determined by an analysis of the forward–backward charge asymmetry  $A_{FB}$ , with respect to the center-of-mass (CM) production angle  $\theta_{CM}$  of the muon pairs (which is usually measured with respect to the axis of the incoming  $e^+$ ).

<sup>1</sup>SLAC: Stanford Linear Accelerator Center.

<sup>2</sup>LEP: Large Electron–Positron Collider.

The differential cross section for muon pair production is:

$$\frac{d\sigma}{d\Omega} = \frac{\alpha^2}{4s} (C_1 (1 + \cos^2\theta_{CM}) + C_2 \cos\theta_{CM}), \quad (2.14)$$

where  $\alpha$  is the fine structure constant,  $s$  is the squared CM energy of the incoming  $e^+/e^-$  and  $C_{1/2}$  are defined as:

$$C_1 = 1 + 2g_V^e g_V^\mu \chi + (g_V^{e2} + g_A^{e2})(g_V^{\mu2} + g_A^{\mu2}) \chi, \quad (2.15)$$

$$C_2 = -4g_A^e g_A^\mu \chi + 8g_V^e g_A^e g_A^\mu \chi^2, \quad (2.16)$$

with  $\chi$  depending on the weak mixing angle, the  $Z$  mass  $M_Z$  and again  $s$ :

$$\chi = \frac{1}{16 \sin^2\theta_W \cos^2\theta_W} \frac{s}{s - M_Z^2}. \quad (2.17)$$

Note that this expression is only valid for  $s \ll M_Z^2$ .

The forward–backward charge asymmetry  $A_{FB}$  is given as:

$$A_{FB} = \frac{F - B}{F + B}, \quad (2.18)$$

where  $F = \int_0^f \frac{d\sigma}{d\theta} d\cos\theta$  and  $B = \int_b^0 \frac{d\sigma}{d\theta} d\cos\theta$  are the number of muons going into the forward (F) or backward (B) direction, respectively. In consequence,  $A_{FB}$  can be expressed via  $C_1$ ,  $C_2$  and the integration bounds  $f$  and  $b$ :

$$A_{FB} = \frac{C_1 (1/3 (f^3 + b^3) + b + f) + 1/2 C_2 (f^2 + b^2)}{C_1 (1/3 (f^3 - b^3) - b + f) + 1/2 C_2 (f^2 - b^2)}, \quad (2.19)$$

which can be simplified by using a symmetric  $\cos\theta_{CM}$  interval  $[-a, a]$ :

$$A_{FB} = \frac{a^2 C_2}{C_1 (1/3 a^3 + 2a)}, \quad (2.20)$$

which, for the whole integration range  $[-1, 1]$ , becomes then:

$$A_{FB} = \frac{3}{8} \frac{C_2}{C_1} \quad (2.21)$$

Note that if the process  $e^+e^- \rightarrow \mu^+\mu^-$  was purely electromagnetic (i.e. only  $\gamma$  exchange, no  $Z$  exchange),  $C_2$  would equal zero and thus the forward–backward asymmetry would vanish.

At Belle energies, the forward–backward asymmetry is in the order of  $10^{-3}$ . To be able to show the running of the weak mixing angle, the forward–backward asymmetry must be measured with a precision of about  $10^{-5}$ , which corresponds to an error on the weak mixing angle in the order of  $10^{-4}$ . Achieving this precision is an extremely challenging task due to systematical uncertainties.

## 2.3 Radiative corrections

Radiative corrections include the afore mentioned higher order loop corrections, as well as initial state radiation (ISR) and final state radiation (FSR). The loop corrections, being absorbed into the effective weak mixing angle via the formfactor  $\kappa(Q)$ , are expected to be in the order of 1.02 at 10 GeV [20]. The corresponding Z pole value is  $\kappa(M_Z) = 1.040$  [20]. It depends mainly on the running of the electromagnetic coupling constant, as well as on the Higgs and top quark masses.

Pure QED corrections, such as ISR and FSR, are calculated up to second order and – as well as weak corrections – included in the Monte–Carlo program *KKMC* [21], which will be introduced in chapter 3.4.

An ISR photon, originating from one of the incoming electrons, usually proceeds very close to the beamline, such that it cannot be detected. It results in a downward shift of the CM energy though, and can thus be identified by measuring the invariant mass of the two muons. The collinearity of the muon pair is not affected by the ISR photon: They are back–to–back in the CM system. The reduced CM energy can give access to one of the lower  $\Upsilon$  resonances. FSR, on the other hand, usually changes the direction of the muon it originates from, such that not only the muon pair’s invariant mass is reduced, but also their collinearity is altered. The most common case is the emission of only one ISR or FSR photon. Multiple photon emission occurs with decreasing probability, but must be taken into consideration, too.

## Chapter 3

# The Belle Experiment

In this chapter, the KEKB Accelerator and the Belle Detector will be introduced (chapters 3.1 and 3.2). Also, Belle's three-level trigger system will be explained in detail in chapter 3.3, followed by a few words on the data handling concept at Belle and the introduction of the Monte Carlo event generator  $\mathcal{KKMC}$  in chapter 3.4.

### 3.1 The KEKB Accelerator

KEKB is a two-ring energy-asymmetric  $e^+e^-$  collider in Tsukuba, Japan. Its layout is depicted in Figure 3.1. A linear accelerator provides the electrons and positrons with the required energies to be fed in bunches into the two separate storage rings, namely the High Energy Ring (HER), containing 8 GeV electrons, and the Low Energy Ring (LER), containing 3.5 GeV positrons. At the interaction point (IP), where the Belle Detector is situated, the bunches collide with a crossing-angle of 22 mrad.

Being a so-called B-Factory, KEKB's design center-of-mass (CM) energy is

$$\sqrt{s} \approx 2\sqrt{E_{HER} \cdot E_{LER}} = 10.58 \text{ GeV}, \quad (3.1)$$

which corresponds to the mass of the  $\Upsilon(4S)$  resonance, just above the  $B\bar{B}$  production threshold. Due to the asymmetric beam energies, all final state particles are produced with a Lorentz boost

$$\beta\gamma \approx \frac{E_{HER} - E_{LER}}{2\sqrt{E_{HER} \cdot E_{LER}}} = 0.425. \quad (3.2)$$

The design instantaneous luminosity of KEKB was  $\mathcal{L} = 10^{34} \text{ cm}^{-2}\text{s}^{-1}$ , yet a world-record peak luminosity of  $\mathcal{L} = 2.11 \cdot 10^{34} \text{ cm}^{-2}\text{s}^{-1}$  was achieved in 2009 [22]. This was possible due to the crab crossing scheme in which the bunches are slightly rotated before the IP, such that they collide head-on (despite the finite crossing angle). Figure 3.2 shows the integrated luminosity collected during Belle operation (1999 – 2010) in comparison with BaBar, a similar experiment at PEP II, a B-Factory at SLAC (1999 – 2008) [23, 24].

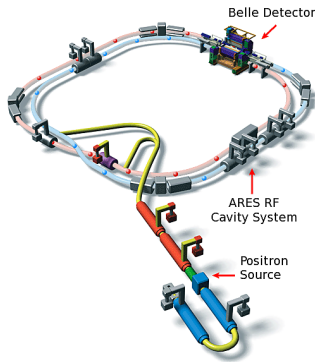


**Figure 3.1:** Schematic drawing of the KEKB accelerator with its two separate rings [25].

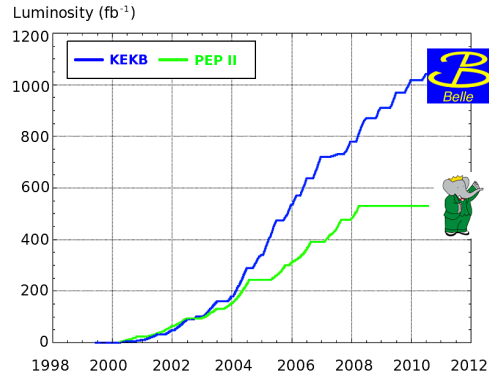


**Figure 3.2:** Integrated Luminosities of KEKB (Belle) and PEP II (BaBar). Belle has collected more than  $1 \text{ ab}^{-1}$  of data [26].

Within the used coordinate system, the positron beam coincides with the  $z$ -axis, with the positrons moving along  $-z$ . The orthogonal  $x$ -axis is also in the horizontal plane, with  $+x$  pointing outwards. The vertical  $y$ -axis completes a right-handed coordinate frame. The polar angle  $\theta$  is measured from the  $+z$ -axis, whereas the azimuthal angle  $\phi$  is measured counterclockwise from the  $+x$ -axis in the  $xy$  plane. The radial distance  $r$  is measured from the  $z$ -axis.

## 3.2 The Belle Detector

Listed in order of radial distance from the interaction point, the Belle detector components are: a three (four)-layer silicon vertex detector (SVD1(SVD2)), a 50-layer central drift chamber (CDC), an array of 1188 aerogel Cherenkov counters (ACC), 128 time-of-flight scintillation counters (TOF/TSC), an electromagnetic calorimeter (ECL) containing 8736 CsI(Tl) crystals, and the  $K_L$  and muon detector (KLM). In addition to the ECL, an Extreme Forward Calorimeter (EFC) is placed in front of the final focusing quadrupole magnet. All components except for the KLM are situated inside a superconducting solenoid providing a central magnetic flux of 1.5 T.

A scheme of the Belle detector is shown in Figure 3.3. The crossing point of the 8.0 GeV electron beam and the 3.5 GeV positron beam is displaced along the beam axis from the geometric center of the detector. This is to account for the afore-mentioned Lorentz boost.

The CDC, ECL and KLM shall now be described in more detail, since those are the three subdetectors this analysis depends on the most:

The **CDC**'s 50 cylindrical drift cell layers are organized into eleven superlayers (six trigger superlayers), with each superlayer containing between three and six either axial or small-angle-stereo layers. Its polar angle coverage is 17.0 to

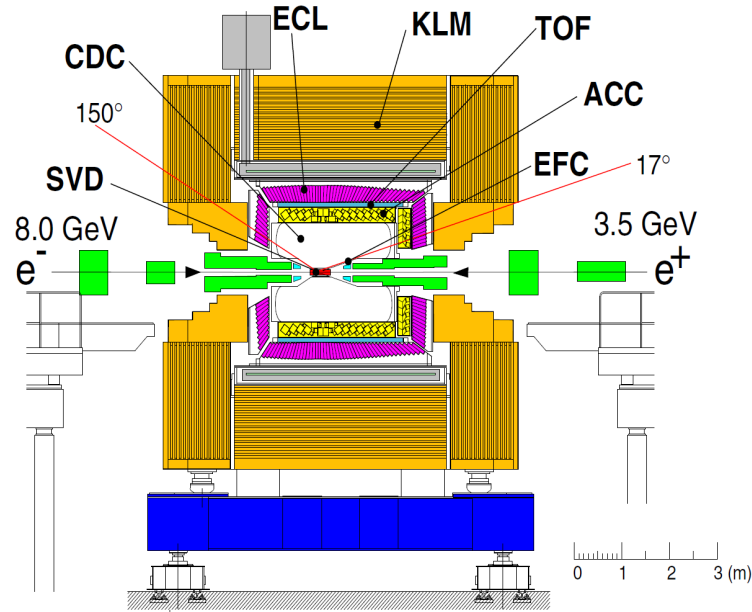


**Figure 3.3:** Schematic drawing of the Belle Detector with its asymmetric design. The CDC acceptance (17 – 150 degrees) is indicated [27].

150.0 degrees. The CDC is essential for an efficient reconstruction of charged particle tracks and for a precise determination of their momenta. Depending on the number of CDC trigger superlayer hits, the tracks are classified as short (track segments in three inner trigger superlayers) or full (track segments in all six trigger superlayers) CDC tracks. In addition, the tracks are projected into and matched with hits in the SVD, if possible. A  $dE/dx$  information is provided by this device as well.

The **ECL**'s 8736 Thallium doped, tower-like shaped CsI crystals are about 30 cm long, with a 5.5 cm $\times$ 5.5 cm (6.5 cm $\times$ 6.5 cm) cross section in the forward (backward) part. The ECL's main purpose is to measure the energy of and identify  $e^{+/-}$  and photons from  $B$  and  $\pi^0$  decays. It covers a polar angular range from 12.0 to 155.1 degrees, with small gaps from 31.4 to 32.2 degrees and from 128.7 to 130.7 degrees.

The **KLM** is comprised of an octagonal-shaped barrel (brl) and two endcaps (fwd/bwd). It consists of alternating layers of 3.7 cm thick glass-electrode resistive plate chamber (RPC) modules and 4.7 cm thick iron plates. Each RPC module contains two independent RPCs arranged back-to-back, sandwiched between orthogonal readout strip planes. The modules are rectangular in the barrel and fan-shaped in the endcaps. The barrel region covers the polar angular range from 51.0 to 117.0 degrees; the two endcaps extend this coverage to between 25.0 and 145.0 degrees. In total, the iron plates provide 3.9 interaction lengths of material for a hadron crossing at normal incidence (in addition to the 0.8

interaction lengths of the ECL). They also serve as the solenoid's return yoke.

Each track which has been reconstructed in the CDC is extrapolated to the KLM. All KLM signals from RPC measurements within 25 cm or  $5\sigma$  of the extrapolated track are associated with it. The expected range of charged hadrons and muons through the material can be estimated using known particle interaction properties. The difference  $\Delta R$  between the measured and the estimated range such as the reduced  $\chi^2$  of the fitted RPC trajectories are used to extract likelihoods  $\mathcal{L}_i^{KLM}$  for a track to be of species  $i$ , with  $i$  being  $\mu$ ,  $\pi$  or  $K$ . The so-called muon ID (muID) is defined as [28]:

$$\text{muID} = \frac{\mathcal{L}_\mu}{\mathcal{L}_\mu + \mathcal{L}_\pi + \mathcal{L}_K}. \quad (3.3)$$

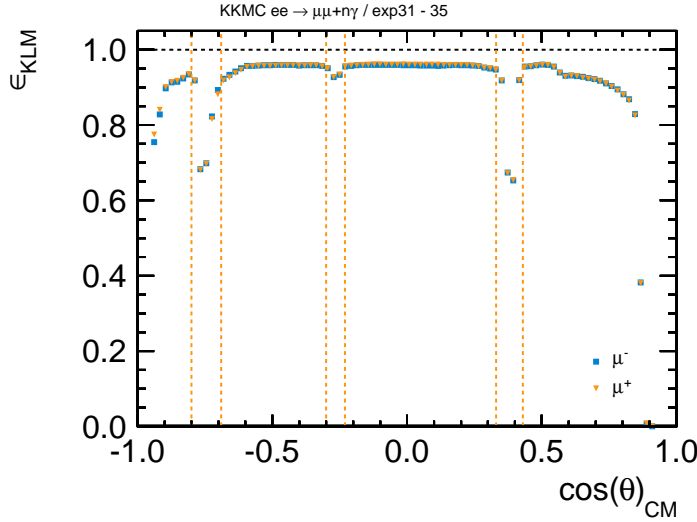


**Figure 3.4:** Angular KLM efficiency as defined in Equation 3.3 for  $\mu^-$  (blue) and  $\mu^+$  (orange). Inefficient regions are marked by the vertical dotted lines.

Figure 3.4 shows the KLM – or rather muID – efficiency for  $e^+e^- \rightarrow \mu^+\mu^- + n\gamma$  events, which is defined as:

$$\epsilon_{\text{KLM}}^{\text{KKMC}} = \frac{\text{number of all preselected events with muID} > 0.8}{\text{number of all preselected events}} \quad (3.4)$$

Marked by the vertical dotted lines are the angular regions in which the KLM efficiency drops because they are not covered completely by the KLM subdetectors. These regions are the transitions from of the KLM barrel to the endcaps (the two big dips) and from the forward part to the backward part of the barrel (small dip). The preselection, requiring two *good*, oppositely charged muon tracks, will be introduced properly in chapter 4.2, the Monte–Carlo event generator  $\text{KKMC}$  used to create the plot in chapter 3.4.

### 3.3 The Belle Trigger System

Belle’s three-level trigger system is comprised of the Level 1 (L1) hardware trigger, the Level 3 (L3) online software trigger and the Level 4 (L4) offline software trigger<sup>1</sup>. Figure 3.5 shows a schematic overview of the Belle trigger system.

If not stated otherwise, all information about the L1 trigger was taken from [29], all information about the L4 trigger from [30]. Information about the L3 trigger has been deduced directly from the source code.

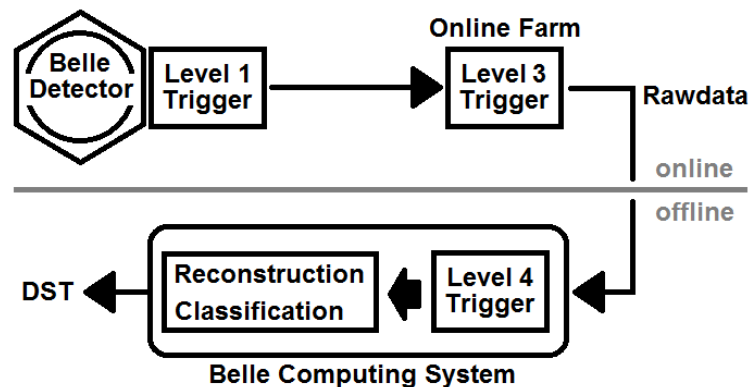


**Figure 3.5:** Overview of the Belle trigger system. Properties of successfully reconstructed events are stored in Data Summary Tapes (DSTs). Adapted from [30].

#### L1 trigger

In principle, the sub-detector trigger system is based on track triggers (CDC/TOF/KLM), energy triggers (ECL/EFC), as well as random triggers. Signals from the sub-detectors are fed into the Global Decision Logic (GDL), where the combined information is used to characterize the event type. The main GDL steps are:

- The **Input Trigger Delay (ITD)**, which adjusts the timing of all incoming sub-trigger signals to meet the maximum latency of  $1.85 \mu\text{s}$ .
- The **Final Trigger Decision Logic (FTDL)**, which combines sub-trigger bits to the actual trigger bits, using logical *and*, *or* and *veto* combinations.
- The **Prescaling and Masking (PSNM)**, where high rate triggers (unrelated to main physics topics) are prescaled with a Prescaling Value (PSV) and unused triggers are disabled.

<sup>1</sup>Since the expression *Level 2 trigger* usually refers to a system between the hardware trigger and an event builder, it was not used but saved for a possible future upgrade of the trigger system.

- The **Timing Decision (TMD)**, where TSC/ECL (*timing triggers*) information is used to generate the final L1 trigger output at  $2.2\ \mu\text{s}$  latency.

### L3 trigger

The L3 trigger is applied to the rawdata before it is saved, i.e. events not passing the L3 stage are lost. Its main purpose is reduction of the trigger rate in order to meet the bandwidth limit. In principle, the L3 data flow is rather similar to the L4 data flow which is described in detail in the next paragraph. The main difference between L3 and L4 is that the L4 tracking is more precise since it has access to calibration data and does not have to be as fast as the L3 trigger.

### L4 trigger

Electrons, positrons and photons from Bremsstrahlung originating from both beams can produce secondary particles whose tracks ususally do not come from the IP. These tracks make up the biggest part of the background. The main task of the L4 trigger is to remove such events in order to further reduce both the trigger rate and the CPU consumption. In order to meet the requirements needed for the task (3 cm  $dz$  resolution, 1 mm  $dr$  resolution, 80 % efficiency for barrel tracks with  $p_t > 300\ \text{MeV}/c$ ) the fast track finder *Fzisan* was introduced. For more details on *Fzisan*, see Appendix A.

Figure 3.6 shows the data flow on the L4 trigger stage. Events with certain L1 trigger bits are passed on directly, as well as events that have been salvaged by the L3 trigger. On the second stage, events with high energy deposition ( $E_{ECL} > 4\ \text{GeV}$ ) are preselected in order to save interesting events containing only uncharged particles. On the third stage, events with at least one *good track* coming from the IP are saved (using *Fzisan*). A *good track* has in this case the following features:

- $p_t > 300\ \text{MeV}/c$ ,
- $|dr| < 1.0\ \text{cm}$ ,
- $|dz| < 4.0\ \text{cm}$ ,

In the end, 1 % of the so far unselected events are saved (L4 salvaging). The rest of the events are not passed on to reconstruction, yet they are not completely deleted but remain on tape in form of rawdata.

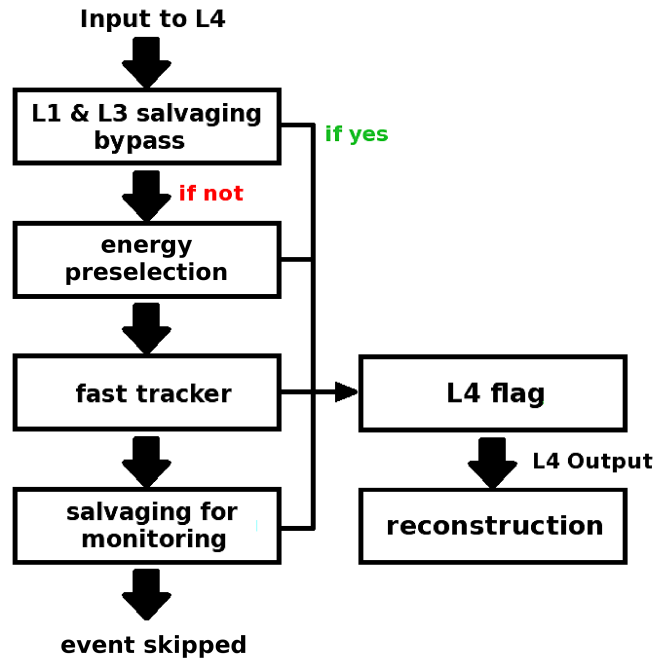


Figure 3.6: Scheme of the L4 data flow. Adapted from [30].

## 3.4 Data Handling and Monte–Carlo Simulation

### Data Handling at Belle

All recorded data is segmented into *experiments* and *runs*, with an *experiment* referring to a time period with a certain detector setup. Only uneven experiment numbers exist, starting with exp5 and ending with exp73. The number of runs per experiment varies from less than 100 to approximately 2000.

Furthermore, the data can be divided into two sets, SVD1 and SVD2. The latter begins with exp31, for which several parts of the inner trackers (the SVD as well as parts of the CDC) have been replaced, after being severely damaged by hard radiation over time [31]. Only certain experiments from the SVD2 set were used for the means of this thesis. All  $\Upsilon(4S)$  on–resonance data from the SVD2 set corresponds to an integrated luminosity of  $571 \text{ fb}^{-1}$ .

The average output rate of the Belle data acquisition (L1) during the SVD2 runs was 8.9 MB/s, corresponding to about 230 events per second [32]. Successfully reconstructed events are stored in Data Summary Tapes (DSTs) and used for detector calibration. During the offline DST processing, raw data and the thus gained calibration constants are used to produce the so–called mini–DST (mdst) files, which can then be used for physics analyses. The logical structure of all files – raw data to mdsts – is defined by the PANTHER event and I/O management package [33], developed by the Belle collaboration. Analyses are performed using

the Belle Analysis Framework (BASF) [34]. A scheme of the offline data flow at Belle is depicted in Figure 3.7.

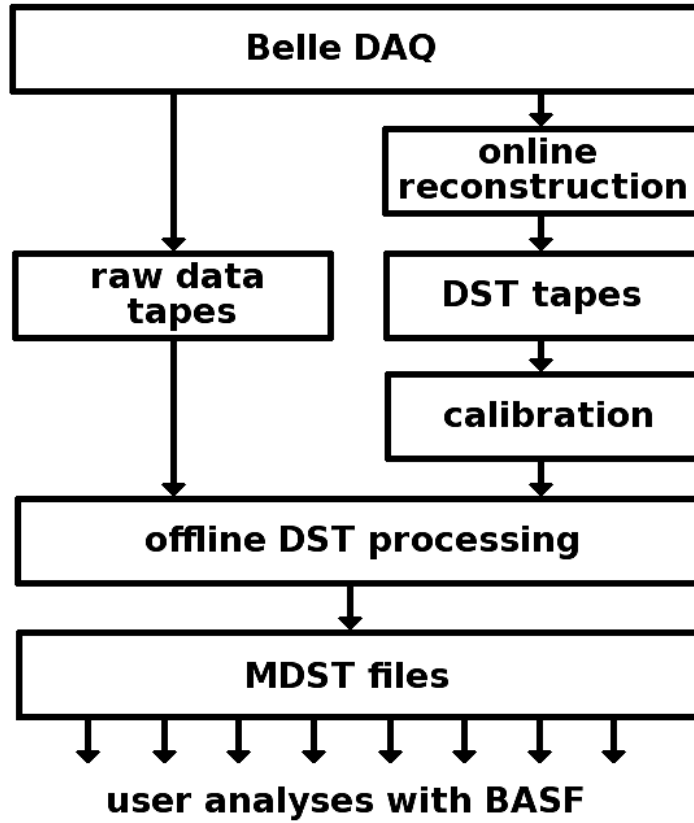


**Figure 3.7:** Scheme of the offline data flow at Belle. DAQ: data acquisition. Figure adapted from [32].

### Monte–Carlo Simulation

SM predictions for  $e^+e^- \rightarrow \mu^+\mu^-$  processes at the precision level of permille and beyond – taking multiple photon emission into account – can only be obtained by using a Monte Carlo (MC) event generator. At Belle, the simulation of  $e^+e^- \rightarrow \mu^+\mu^- + n\gamma$  interactions was done with the  $\mathcal{K}\mathcal{K}\mathcal{M}\mathcal{C}$  event generator for two–fermion final states in  $e^+e^-$  collisions in the presence of multiphoton ISR [21]. The  $e^+e^- \rightarrow \tau^+\tau^- + n\gamma$  events used for background studies, were also generated with  $\mathcal{K}\mathcal{K}\mathcal{M}\mathcal{C}$ . Within  $\mathcal{K}\mathcal{K}\mathcal{M}\mathcal{C}$ , ISR and FSR are described in the in the framework of exclusive coherent exponentiation, which treats QED interferences, narrow resonances and infrared cancellations correctly to infinite order. The beam spread is accounted for as well.

For other background channels other event generators were used, for example AAFHB [35] and Babayaga NLO [36, 37, 38, 39, 40].

The events are generated in the CM frame and then boosted to the laboratory frame before being passed on to the detector and trigger simulations. Also, all MC samples contain beam background taken from randomly triggered real data.

The impact of the beam energy smearing on  $A_{\text{FB}}$  was also investigated analytically: For  $\sqrt{s}$  a Gaussian profile with  $\sigma_{\sqrt{s}} = 0.0049 \text{ GeV}$  was assumed, which was calculated via Gaussian error propagation from the uncertainties on  $E_{\text{HER}}$  and  $E_{\text{LER}}$ . With  $A_{\text{FB}}$  depending on  $\sqrt{s}$ , this leads to a Gaussian shape of  $A_{\text{FB}}$  with a  $\sigma_{A_{\text{FB}}}$  of  $0.68 \times 10^{-5}$ , which is even larger than the expected statistical uncertainty at Belle II.

Fortunately, the change of  $A_{\text{FB}}$  due to the Gaussian energy profile and the effect of assuming an inaccurate  $\sqrt{s}$  for boosting events from the laboratory system back into the CM system for the analysis are almost fully anti-correlated. This could be demonstrated with the tree-level MC event generator *tegen*, with which  $\sigma_{A_{\text{FB}}}$  was determined to be smaller than  $1.0 \times 10^{-6}$  [41]. The same limit was given for angular smearing (effects from the uncertainty on the beam crossing-angle).

# Chapter 4

## Analysis

The main goal of this thesis is a thorough trigger investigation. Since the actual trigger efficiency depends on the respective event selection, the first task was to find adequate selection criteria in order to select clean  $e^+e^- \rightarrow \mu^+\mu^-$  events. The most important background channels will be introduced in chapter 4.1, the event selection in chapter 4.2. Based on this event selection, the L1 trigger efficiency will be determined first on MC level, then also with experimental data, using the Orthogonal Trigger method (chapter 4.3).

### 4.1 Background Events

The process  $e^+e^- \rightarrow \mu^+\mu^-$  (signal process, also denoted as *mumu* within this thesis) has a cross section of about 1.1 nb at  $\sqrt{s} = 10.58$  GeV [42]. Assuming an integrated luminosity of  $0.5 \text{ ab}^{-1}$ , this corresponds to roughly half a billion muon pairs. In general, muons have a very clear signature and can be identified rather easily as they have a low energy deposition  $dE/dx$  and thus usually create long, mostly scattering-free tracks in the detector. There are several processes, though, which also have a dilepton final state and must be distinguished carefully from the signal process.

- $e^+e^- \rightarrow e^+e^- + n\gamma$  (also denoted as *Bhabha* within this thesis)  
With a cross section of about 119.4 nb (angular range: 15–165 degrees in the CM system) [36, 37, 38, 39, 40], this background channel is – before the respective PID cuts – by far the most dominant one. Electrons and muons can be distinguished, for example, by their different relative amount of energy they deposit in the ECL or by using KLM information.
- $e^+e^- \rightarrow e^+e^-\mu^+\mu^-$  (also denoted as *eemm* within this thesis)  
There are several leading order diagrams describing this process, each of them has two internal photons. The final state contains four, not two particles, but as the  $e^\pm$  pair tends to proceed relatively close to the beamline after the collision, they can very often not be detected. Yet, as they often carry away a large part of the energy, the remaining muons can be identified as

background by momentum or invariant mass cuts. For  $m_{\text{inv}}(\mu\mu) > 0.5 \text{ GeV}$ , the cross section of this process is 18.9 nb [35].

- $e^+e^- \rightarrow \tau^+\tau^- + n\gamma$  (also denoted as *tautau* within this thesis)

The cross section of this process is slightly smaller than that of the signal process, about 0.9 nb at  $\sqrt{s} = 10.58 \text{ GeV}$  [42]. With a branching ratio of about 17.4% [43], a tauon decays via  $\tau^\pm \rightarrow \bar{\nu}_\tau/\nu_\tau + \nu_\mu/\bar{\nu}_\mu + \mu^\pm$ . If both tauons decay in this manner, they again leave two muons (and four undetectable particles) in the detector. Those can be identified as background by momentum or invariant mass cuts, as well.

- **Other Background Channels**

Other background channels which are checked explicitly are:

$e^+e^- \rightarrow u\bar{u}$  ( $d\bar{d}, s\bar{s}, c\bar{c}$ ) (denoted as *uds* or *charm*) and

$e^+e^- \rightarrow \Upsilon(4S) \rightarrow B^+B^-(B^0\bar{B}^0)$  (denoted as *charged* or *mixed*).

A vast majority of these events will already be removed by demanding exactly two charged tracks.

The decay  $\Upsilon(4S) \rightarrow \mu^+\mu^-$  has a branching fraction of less than  $1.6 \times 10^{-3} \%$  and is not considered relevant for this analysis. Radiative returns of lower resonances due to initial state radiation can occur. The corresponding branching fractions are in the order of a few percent, yet they are not treated explicitly within this thesis either. However, they should be considered in any continuative analysis.

- **Background from Cosmic Muons**

Cosmic muons enter the detector from above and, if passing very close to the IP, can be reconstructed as two oppositely charged muon tracks coming from the IP. Since the cosmic muons are reconstructed back-to-back in the laboratory system and not in the CM system like real muon pairs originating at the IP, they can be suppressed by collinearity cuts. Furthermore, their time-of-flight information can be used to identify them as background. Cosmic muons are not treated explicitly within this thesis though.

## 4.2 Event Selection

In the following plots, different selection criteria have been tested using MC generated events from exp35, corresponding to an integrated luminosity of  $7908 \text{ pb}^{-1}$  which is 1.4% of the available statistics from data (SVD2,  $\Upsilon(4S)$ , on-resonance).

All events were preselected using the following criteria:

- the event contains exactly two *good muon tracks*,
- the sum of the charges of the two tracks equals zero.

A *good muon track* is in this case defined as a charged track reconstructed under a muon hypothesis, fulfilling the following criteria:

- has a minimum transverse momentum  $p_t > 0.1 \text{ GeV}$ ,
- has a maximum distance from IP  $dz < 5 \text{ cm}$  and  $dr < 0.5 \text{ cm}$ ,
- lies within CDC acceptance:  $-0.8660 < \cos \theta_{\text{lab}} < 0.9563$ ,

This selection yields an efficiency of

$$\epsilon_{\text{preSEL}} = \frac{\text{all preselected MC generated signal events}}{\text{all MC generated signal events}} = (70.53 \pm 0.02) \%. \quad (4.1)$$

The stated uncertainty is purely statistical (Bayesian,  $1\sigma$  C.L.), as are all uncertainties in this thesis.

The following main selection consists of two individual steps: The first goal was the elimination of photons by cuts on the energy  $E_{\gamma \text{ max}}$  of the most energetic photon in the event, the invariant mass  $m_{\text{inv}}$  and/or the collinearity  $\text{collin}_{\text{CM}}$  of the two tracks. The second goal was to further suppress events from the previously introduced background channels, especially Bhabha events.

### Main Selection Step One: Photons

As the complete absence of photons does not occur, any reconstructed photon must have a reconstructed energy of **at least 25 MeV** in order to be viewed as a photon within this analysis (within the MC, the cut-off is at about 21 MeV). On MC basis, the provided MCTruth information can be used to distinguish between primary photons (from  $e^+e^- \rightarrow \mu^+\mu^- + n\gamma$  events) and photons from beam background in order to check the purity of the sample. Note that only successfully reconstructed photons are accounted for. The  $E_{\gamma \text{ max}}$  distribution of all preselected events and all preselected events without primary photons with more than 25 MeV is shown in Figure 4.1. Figure 4.2 shows the selection efficiency  $\epsilon_{\text{sel}}$ , the purity and their product for  $E_{\gamma \text{ max}}$  cut values between 100 MeV and 1.2 GeV. Selection efficiency and purity are in this case defined as:

$$\epsilon_{\text{sel}}^{E_{\gamma \text{ max}}} = \frac{\text{nr. of preselected events with } E_{\gamma \text{ max}} < \text{cut value}}{\text{nr. of all preselected events}} \quad (4.2)$$

$$\text{purity} = \frac{\text{nr. of preselected events with } E_{\gamma \text{ max}} < \text{cut value} \ \& \ \text{no primary photons}}{\text{nr. of preselected events with } E_{\gamma \text{ max}} < \text{cut value}} \quad (4.3)$$

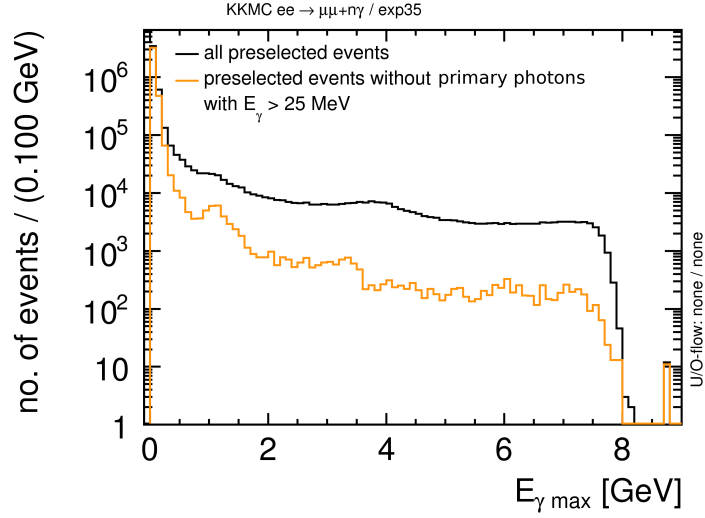


**Figure 4.1:**  $E_{\gamma \text{ max}}$  distribution of all preselected events (black) and preselected events containing only photons from beam background (orange).

The aim is to maximize the purity while keeping the selection efficiency loss at a reasonable level. The product  $\text{purity} \times \epsilon_{\text{sel}}^{E_{\gamma \text{ max}}}$  should be maximized, too, and also show stability with respect to variation of the cut value. A local maximum cannot be found in this case. Therefore, the cut value is chosen to be 300 MeV, where  $\epsilon_{\text{sel}}^{E_{\gamma \text{ max}}} = (86.60 \pm 0.02) \%$  and  $\text{purity} = (90.61 \pm 0.01) \%$ .

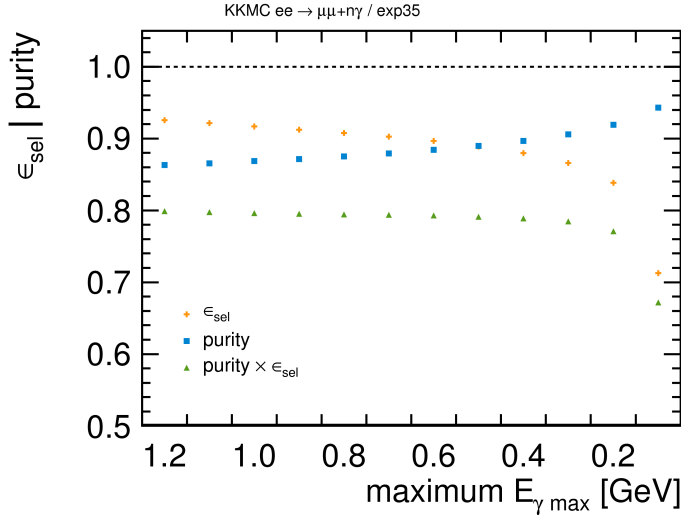


**Figure 4.2:** Selection efficiency  $\epsilon_{\text{sel}}$  (orange), purity (blue) and their product (green) for different  $E_{\gamma \max}$  cut values. The statistical uncertainties are too small to be seen in this plot.

In addition, the effects of  $m_{\text{inv}}$  and  $\text{collin}_{\text{CM}}$  cuts were investigated. The distributions of these quantities are shown in Figures 4.3 and 4.5, the selection efficiencies after the corresponding cuts in Figures 4.4 and 4.6. The cuts on  $m_{\text{inv}}$  are to be understood as symmetric cuts around the CM energy  $\sqrt{s}$ . The following cut values were considered reasonable:

- $m_{\text{inv}} = (1 \pm 15 \%) \times \sqrt{s}$ , where  $\epsilon_{\text{sel}}^{m_{\text{inv}}} = (81.64 \pm 0.02) \%$
- $\text{collin}_{\text{CM}} = 165$  degrees, where  $\epsilon_{\text{sel}}^{\text{collin}_{\text{CM}}} = (83.81 \pm 0.02) \%$

A combination of these two cuts yields  $\epsilon_{\text{sel}}^{m_{\text{inv}} \& \text{collin}_{\text{CM}} \text{ cuts}} = (81.17 \pm 0.02) \%$ , which implies that the invariant mass cut already covers most of the events which would be removed by the collinearity cut, such that the latter has only small influence. Therefore, only the invariant mass cut will be applied. Combining it with the  $E_{\gamma \max}$  cut, the selection efficiency with respect all preselected events is  $\epsilon_{\text{sel}}^{E_{\gamma \max} \& m_{\text{inv}} \text{ cuts}} = (75.46 \pm 0.02) \%$ .

At this point, the total selection efficiency is:

$$\epsilon_{\text{sel}}^{\text{presel} \& E_{\gamma \max} \& m_{\text{inv}} \text{ cuts}} = \epsilon_{\text{presel}} \times \epsilon_{\text{sel}}^{E_{\gamma \max} \& m_{\text{inv}} \text{ cuts}} = (53.22 \pm 0.02) \%. \quad (4.4)$$

Note that a large part of the events not selected by these criteria lie outside the geometrical acceptance of the detector.

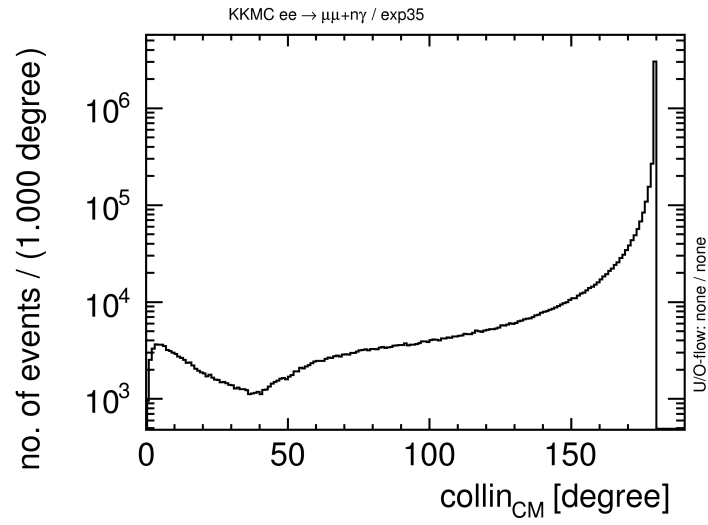


**Figure 4.3:** collin<sub>CM</sub> distribution of all preselected events, peaking at 180 degrees.

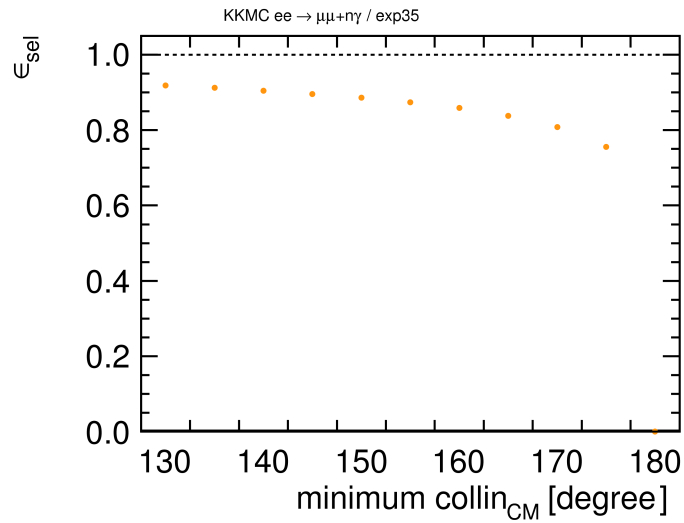


**Figure 4.4:** Selection efficiency  $\epsilon_{\text{sel}}$  for different collin<sub>CM</sub> cut values. The statistical uncertainties are too small to be seen in this plot.

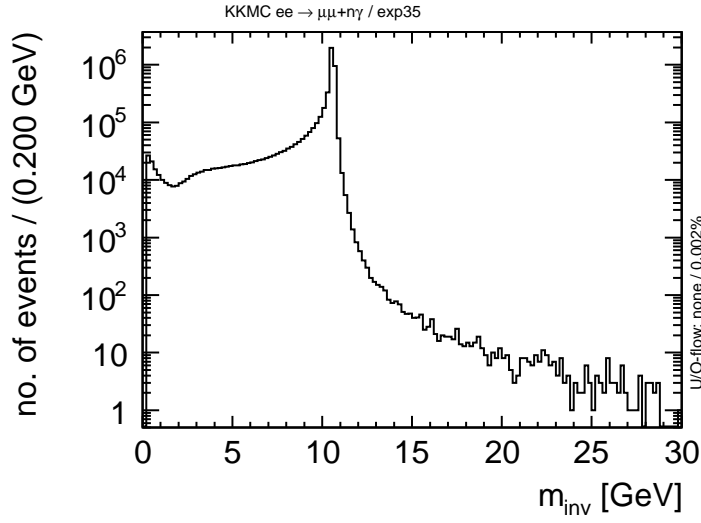


**Figure 4.5:**  $m_{\text{inv}}$  distribution of all preselected events, peaking at the CM energy  $\sqrt{s}$ .

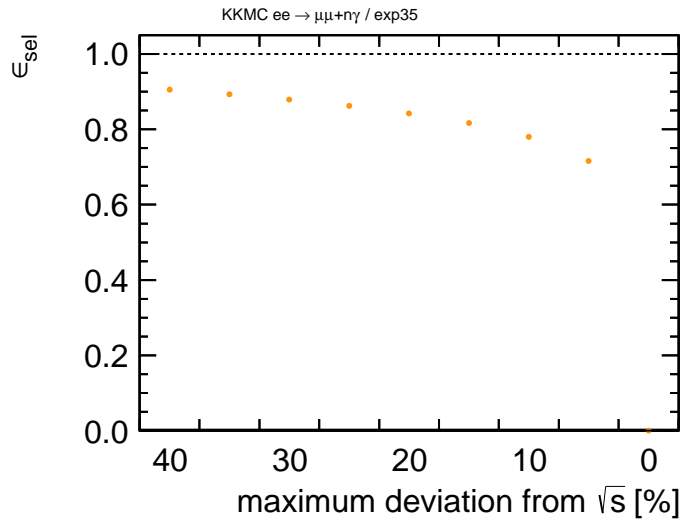


**Figure 4.6:** Selection efficiency  $\epsilon_{\text{sel}}$  for different  $m_{\text{inv}}$  cut values. The statistical uncertainties are too small to be seen in this plot.

### Main Selection Step Two: Bhabha and Other Background Events

The second main selection step concerns the previously introduced background channels. They are suppressed already very efficiently by the previous cuts as shown in Table 4.1. The remaining eemm and tautau background events cannot be removed by  $p_{(t)\text{Lab}/\text{CM}}^{(max)}$  or any similar cuts without further reducing the signal selection efficiency. With eemm/tautau selection efficiencies at the permille level, their suppression is already considered sufficient anyway. Cuts on the muon and electron ID, as well as on the ECL energy deposition of a particle over its momentum  $\frac{E_{ECL}}{|p|_{\text{Lab}}}$ , can be used to distinguish between electrons and muons and thus suppress the background from Bhabha scattering.

The Bhabha events were generated with the MC program Babayaga NLO [36, 37, 38, 39, 40]. They correspond to run01 of exp35 (prescaled with a factor of  $\frac{12.5}{119.4}$ ) and were generated for for a reduced angular range only – due to huge cross sections at small angles. Therefore, no preselection efficiency comparable to the other channels can be given for Bhabha events. Yet, as only tracks within CDC acceptance ( $\theta_{\text{CM}} = 25.5 - 159.9$  degrees) are preselected anyway, all selection steps after the preselection are again comparable. The same is true for eemm events, which were generated with the MC program AAFHB [35], although here, in addition, only events with  $m_{\text{inv}}(\mu\mu) > 0.5$  GeV are regarded.

**Table 4.1:** Selection efficiencies for signal and background MCs for the preselection, the main selection step 1 and their combination. The stated uncertainties and limits are Bayesian.

MC	$\epsilon_{\text{pre sel}} [\%]$	$\epsilon_{\text{sel}}^{E_{\gamma \text{ max}} \& m_{\text{inv}} \text{ cuts}} [\%]$	$\epsilon_{\text{sel}}^{\text{pre sel} \& E_{\gamma \text{ max}} \& m_{\text{inv}} \text{ cuts}} [\%]$
mumu	$70.53 \pm 0.02$	$75.46 \pm 0.02$	$53.22 \pm 0.02$
eemm <sup>a b</sup>	–	$(7.27 \pm 0.08) \times 10^{-2}$	–
tautau	$53.71 \pm 0.02$	$(1.30 \pm 0.02) \times 10^{-1}$	$(0.70 \pm 0.01) \times 10^{-1}$
uds	$2.43 \pm 0.01$	$(0.12 \pm 0.03) \times 10^{-1}$	$(0.18_{-0.07}^{+0.08}) \times 10^{-3}$
charm	$1.73 \pm 0.01$	$< 0.02 \times 10^{-1}$	$< 0.04 \times 10^{-3}$
charged	$(2.41 \pm 0.04) \times 10^{-1}$	$< 0.03$	$< 0.08 \times 10^{-3}$
mixed	$(2.06 \pm 0.04) \times 10^{-1}$	$< 0.04$	$< 0.09 \times 10^{-3}$
Bhabha <sup>a</sup>	–	$69.32 \pm 0.15$	–

<sup>a</sup> $\epsilon_{\text{pre sel}}$  undefined. See text above for more details.

<sup>b</sup>For  $m_{\text{inv}}(\mu\mu) > 0.5$  GeV only.

**(1) Particle Identification: muID and eID**

With respect to particle identification, it should be sufficient to make a *loose* muon selection, not requiring both reconstructed muons to be identified as muons (muID larger than some cut value  $a$ ), but only one identified as a muon and the other one not as an electron (eID smaller than some cut value  $b$ ):

$$[\text{muID}(\mu^+) > a \ \&\& \ \text{eID}(\mu^-) < b] \ || \ [\text{muID}(\mu^-) > a \ \&\& \ \text{eID}(\mu^+) < b] \quad (4.5)$$

Asking for both muons to have a muon ID would result in an efficiency loss due to uncovered areas in the KLM. Muon and electron ID for the reconstructed  $\mu^-$  are shown in Figures 4.7 and 4.8. Apparently, the lower cut  $b$  on the electron ID should be chosen to be rather tight: Only  $(0.0125 \pm 0.0006) \%$  of the reconstructed muons from the mumu MC are identified as electrons (have an eID  $> 0.0$ ).

At the same time, only  $(0.0032^{+0.0030}_{-0.0018}) \%$  of the reconstructed tracks from the Bhabha MC are identified as muons (have a muID  $> 0.0$ ). Therefore, a rather low muon ID cut is sufficient, too. Using the selection criterion defined in Equation 4.5 with  $a = b = 0.1$ , the selection efficiencies (with respect to all selected events after main selection step 1) are:

- for the mumu MC:  $\epsilon_{\text{sel}}^{\text{muID/eID cuts}} = (99.411 \pm 0.004) \%$
- for the Bhabha MC:  $\epsilon_{\text{sel}}^{\text{muID/eID cuts}} < 0.002 \%$

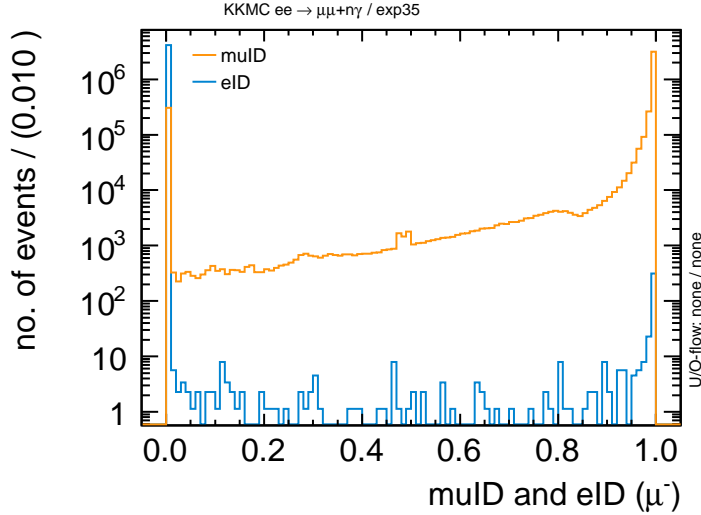


**Figure 4.7:** Muon and electron ID distributions for mumu MC after main selection step 1.

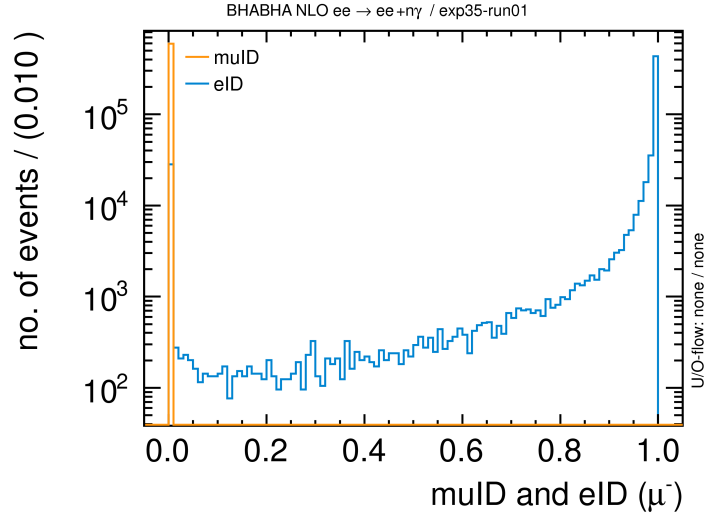


**Figure 4.8:** Muon and electron ID distributions for Bhabha MC after main selection step 1.

## (2) Energy Deposition: $E_{\text{ECL}}/|p|_{\text{Lab}}$

As the CDC and ECL cover have a larger geometrical acceptance than the KLM, it is considered to use the quantity  $E_{\text{ECL}}/|p|_{\text{Lab}}$  in order to distinguish between muons and electrons, instead of the muon and electron IDs. Furthermore, the quantity allows an investigation of correlations and systematical uncertainties, since the muID is provided by the KLM, a very dominant subdetector with respect to the trigger logic of  $e^+e^- \rightarrow \mu^+\mu^- + n\gamma$  events.

As minimal ionizing particles, muons will keep most of their energy when passing through any kind of material and thus have a small  $E_{\text{ECL}}/|p|_{\text{Lab}}$  ratio. Electrons however will usually deposit most of their energy in the ECL, such that  $E_{\text{ECL}}/|p|_{\text{lab}}$  is close to 1. This can be seen in Figure 4.9. Note that the Figure shows the  $E_{\text{ECL}}/|p|_{\text{Lab}}$  distribution for only one reconstructed muon, whereas the cut will be applied on both reconstructed muons at the same time. A cut at  $E_{\text{ECL}}/|p|_{\text{Lab}} = 0.4$  yields:

- for the mumu MC:  $\epsilon_{\text{sel}}^{\text{E/p cuts}} = (99.938 \pm 0.001) \%$
- for the Bhabha MC:  $\epsilon_{\text{sel}}^{\text{E/p cuts}} < 0.002 \%$

This selection criterion will be used for the following trigger studies. An overview of all applied selection criteria can be found in Table 4.2. The total selection efficiencies for mumu and the most dominant background channels are listed in Table 4.3. The stacked histograms in Figures 4.10 and 4.11 allow an comparison of the different contributions from the mumu, Bhabha, eemm and tautau MCs before and after the  $E_{\text{ECL}}/|p|_{\text{Lab}}$  cut. The number of eemm and tautau events can hardly be reduced by this cut (but is already quite low, note the logarithmic

scale), whereas the Bhabha background is reduced dramatically by it: No Bhabha events at all can be found after applying all cuts. With higher statistics the limit could be further reduced.

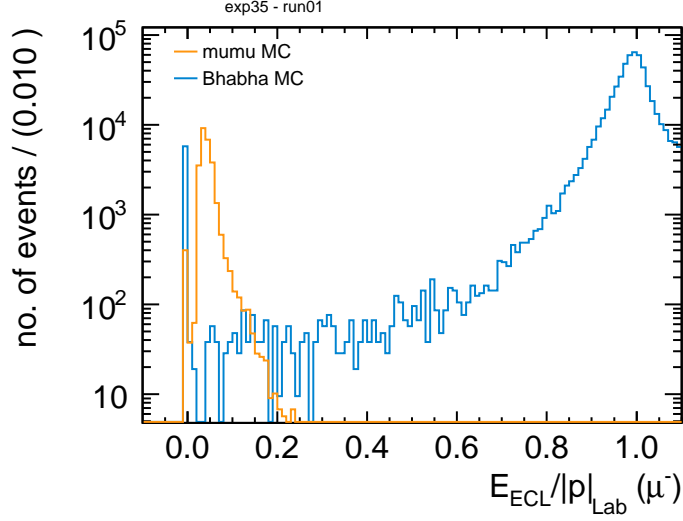


**Figure 4.9:**  $E_{\text{ECL}}/|p|_{\text{Lab}}$  distribution after main selection step 1 for both mumu and Bhabha MCs.

**Table 4.2:** Overview of all applied selection criteria.

Selection Step	Selection Criteria
<b>preselection</b>	exactly two good muon tracks total charge = 0
<b>main selection</b>	$m_{\text{inv}} = (1 \pm 15\%) \times \sqrt{s}$
step 1	$E_{\gamma \text{ max}} < 300 \text{ MeV}$
step 2	$E_{\text{ECL}}/ p _{\text{Lab}}(\mu^-) < 0.4 \ \&\& \ E_{\text{ECL}}/ p _{\text{Lab}}(\mu^+) < 0.4$

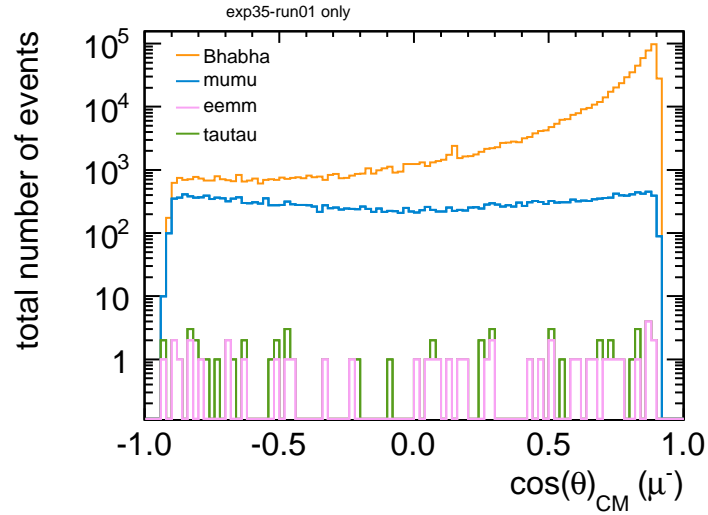


**Figure 4.10:** Number of events in exp35–run01 after preselection,  $E_{\gamma \max}$  and  $m_{\text{inv}}$  cuts, but before  $\frac{E_{FCL}}{|p|_{\text{Lab}}}$  cuts.

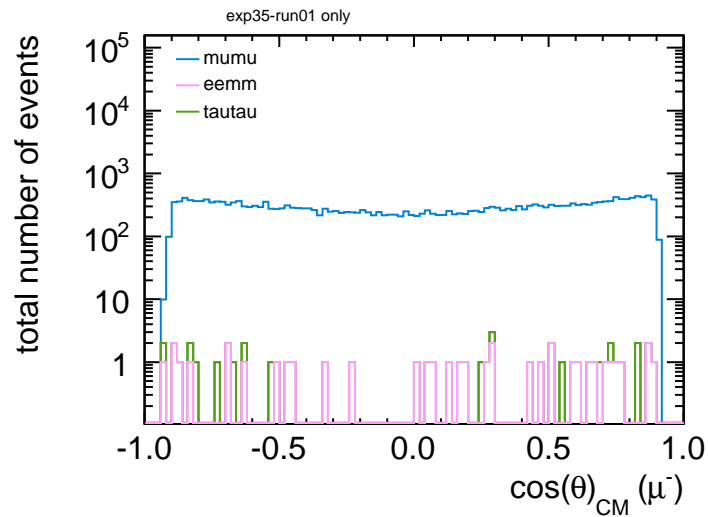


**Figure 4.11:** Number of events in exp35–run01 after all cuts.

**Table 4.3:** Total selection efficiencies (using the selection criteria from Table 4.2) for signal and background MCs. Only for channels with  $\epsilon_{\text{sel}}^{\text{pre sel } \& E_{\gamma \text{ max } \& m_{\text{inv cuts}}} \neq 0$ . mumu/tautau/uds: with respect to all MC generated events. eemm/Bhabha: with respect to all preselected events. Bhabha: exp35–run01 only. Rest: full exp35. See text above for more details.

MC	$\epsilon_{\text{total sel}} [\%]$
mumu	$53.19 \pm 0.02$
eemm	$(5.83 \pm 0.08) \times 10^{-2}$
tautau	$(3.52 \pm 0.08) \times 10^{-2}$
uds	$(0.17^{+0.06}_{-0.05}) \times 10^{-3}$
Bhabha	$< 0.02 \times 10^{-2}$

## 4.3 Determination of L1 Trigger Efficiencies

### 4.3.1 Monte – Carlo based Trigger Efficiencies

When working with MC, on which trigger simulations have been run, the (sub)trigger efficiency  $\epsilon_{\text{trg } i}^{\text{MC}}$  for a certain L1 (sub)trigger bit  $i$  can be defined as:

$$\epsilon_{\text{L1 trg } i}^{\text{MC}} = \frac{\text{number of all selected events with (sub)trigger bit } i \text{ hit}}{\text{number of all selected events}}. \quad (4.6)$$

This definition cannot be used for experimental data because – as only triggered events can be reconstructed and saved – the number of all selected events is unknown. It is a suitable definition for a basic trigger investigation and MC consistency checks though.

Due to the topology of the signal event, the `klm_opn` trigger bit (#24) is of particular interest and importance for this analysis. It requires a `cdc_open` subtrigger hit and a `klm_bwd`, `klm_fwd` or `klm_br1` subtrigger hit.

The `cdc_open` condition requires two CDC tracks (at least one full) with an opening angle of at least 135 degrees in the  $r - \phi$  plane. Since only one of the two muons must trigger one of the KLM subtriggers, and a majority of the events should automatically fulfil the opening angle condition, the `klm_opn` efficiency was expected and confirmed to be relatively high. The `klm_b2b` trigger bit (#25) requires an even larger opening angle. Its efficiency is therefore slightly smaller.

Other prominent trigger bits and angular distributions are given below. Prominent means they trigger often and are not prescaled (except for `klm_tsc` with a PSV of 10) or have a promising subtrigger bit combination (e.g. high efficiencies, constant efficiencies in certain angular regions, orthogonal to other triggers). Many of them are two – track triggers demanding one or two short (*s*) or full (*f*) CDC tracks. Table 4.4 shows an overview of the most important L1 trigger bits and their efficiencies with respect to all selected events, both for single trigger bits and for combinations of two trigger bits.

**Table 4.4:** L1 Trigger efficiencies  $\epsilon_{\text{trg } i}^{\text{numu MC exp31-35}}$  [%] with respect to all selected events for single trigger bits (diagonal entries) and for combinations of two triggers. Note that these are total efficiencies for the whole CDC acceptance range.

	<b>ff_t2oc</b>	<b>ff_t2oc2</b>	<b>hie</b>	<b>klm_opn</b>
<b>ff_t2oc</b>	<b>40.80 ± 0.01</b>	40.32 ± 0.01	(6.10 ± 0.02) × 10 <sup>-1</sup>	40.78 ± 0.01
<b>ff_t2oc2</b>	40.32 ± 0.01	<b>40.32 ± 0.01</b>	(6.09 ± 0.02) × 10 <sup>-1</sup>	40.30 ± 0.01
<b>hie</b>	(6.10 ± 0.02) × 10 <sup>-1</sup>	(6.09 ± 0.02) × 10 <sup>-1</sup>	<b>(12.20 ± 0.02) × 10<sup>-1</sup></b>	(9.92 ± 0.02) × 10 <sup>-1</sup>
<b>klm_opn</b>	40.78 ± 0.01	40.30 ± 0.01	(9.92 ± 0.02) × 10 <sup>-1</sup>	<b>81.46 ± 0.01</b>
<b>klm_b2b</b>	40.78 ± 0.01	40.30 ± 0.01	(9.91 ± 0.02) × 10 <sup>-1</sup>	81.44 ± 0.01
<b>loe_fs_o</b>	9.48 ± 0.01	9.47 ± 0.01	(9.89 ± 0.02) × 10 <sup>-1</sup>	15.62 ± 0.01
<b>loe_fs_to</b>	9.48 ± 0.01	9.47 ± 0.01	(9.59 ± 0.02) × 10 <sup>-1</sup>	15.16 ± 0.01
<b>klm_tsc<sup>a</sup></b>	24.63 ± 0.01	24.41 ± 0.01	(5.09 ± 0.02) × 10 <sup>-1</sup>	28.51 ± 0.01

	<b>klm_b2b</b>	<b>loe_fs_o</b>	<b>loe_fs_to</b>	<b>klm_tsc<sup>a</sup></b>
<b>ff_t2oc</b>	40.78 ± 0.01	9.48 ± 0.01	9.48 ± 0.01	24.63 ± 0.01
<b>ff_t2oc2</b>	40.30 ± 0.01	9.47 ± 0.01	9.47 ± 0.01	24.41 ± 0.01
<b>hie</b>	(9.91 ± 0.02) × 10 <sup>-1</sup>	(9.89 ± 0.02) × 10 <sup>-1</sup>	(9.59 ± 0.02) × 10 <sup>-1</sup>	(5.09 ± 0.02) × 10 <sup>-1</sup>
<b>klm_opn</b>	81.44 ± 0.01	15.62 ± 0.01	15.16 ± 0.01	28.51 ± 0.01
<b>klm_b2b</b>	<b>81.44 ± 0.01</b>	15.61 ± 0.01	15.16 ± 0.01	28.50 ± 0.01
<b>loe_fs_o</b>	15.61 ± 0.01	<b>15.70 ± 0.01</b>	15.23 ± 0.01	6.55 ± 0.01
<b>loe_fs_to</b>	15.16 ± 0.01	15.23 ± 0.01	<b>15.23 ± 0.01</b>	6.55 ± 0.01
<b>klm_tsc<sup>a</sup></b>	28.50 ± 0.01	6.55 ± 0.01	6.55 ± 0.01	<b>15.23 ± 0.01</b>

<sup>a</sup>After FTDL, before PSNM. PSV = 10.

```

#1      ff_t2oc = ncd_r_full>1 & cdc_open & tsc_ge2 & !csi_bb & csi_timing
#12     hie = e_high & !csi_bb & !csi_cosmic
#24    klm_opn = (klm_brl || klm_fwd || klm_bwd) & cdc_open
#25    klm_b2b = (klm_brl || klm_fwd || klm_bwd) & cdc_bb
#58    klm_tsc = (klm_brl || klm_fwd || klm_bwd) & tsc_pat
#93    loe_fs_o = e_low & ncd_r_short>1 & ncd_r_full>0 & cdc_open & !csi_bb
#98    ff_t2oc2 = ncd_r_full>1 & cdc_open & tsc_ge2 & !csi_bb & nicl>1
#110   loe_fs_to = e_low & ncd_r_short>1 & ncd_r_full>0 & cdc_open & !csi_bb & tsc_ge1

```

klm\_brl/fwd/bwd = KLM barrel / forward endcap / backward endcap trigger  
ncd\_r\_short/full = number of short/full CDC  $R-\phi$  tracks  
cdc\_open = opening angle cut ( $> 135$  degrees)  
cdc\_bb = 1–7 back to back tracks with 64 segm. in the CDC  $R-\phi$  plane  
csi\_bb/cosmic = ECL Bhabha/cosmic veto trigger  
nicl = number of isolated clusters on ECL  
e\_low/high = ECL low/high energy trigger ( $> 0.5/1.0$  GeV)  
tsc\_ge1[2] = number of TSC hits  $\geq 1$  [2]  
tsc\_pat = TOF hit pattern (1–3 back to back)

The angular trigger efficiencies in the following Figures 4.12 to 4.31 are given with respect to all selected MC generated events and before PSNM, according to Equation 4.6. Individual plots are shown for the reconstructed  $\mu^+$  and  $\mu^-$  and for the CM and the laboratory frame. An explanation why only exp31 to exp35 were used is given afterwards.

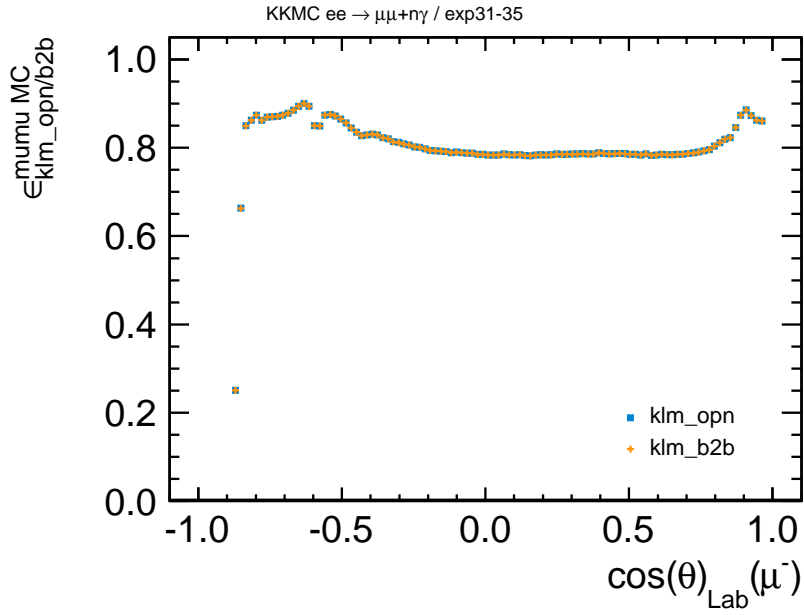


Figure 4.12:  $\cos(\theta)_{\text{Lab}}$  distribution of  $\epsilon_{\text{klm\_opn}}^{\text{mumu MC}}$  (PSV=1) and  $\epsilon_{\text{klm\_b2b}}^{\text{mumu MC}}$  (PSV=1) for  $\mu^-$ .

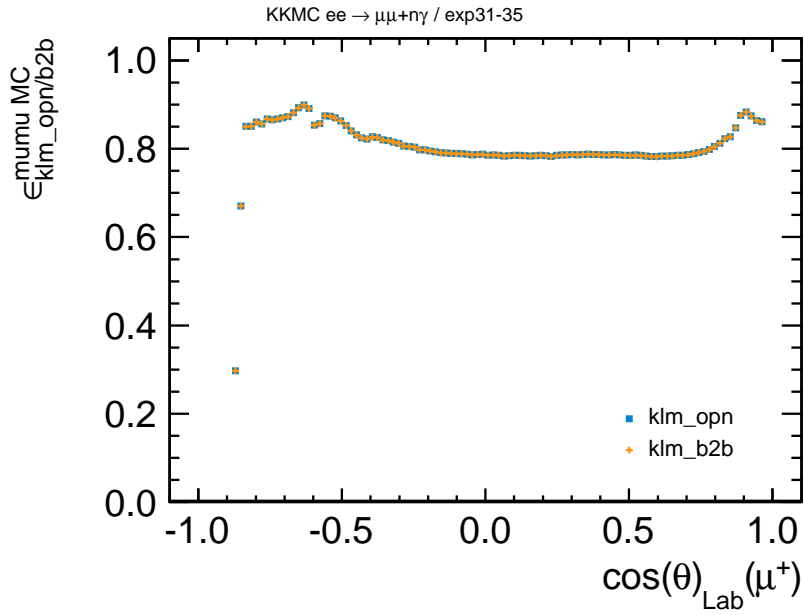
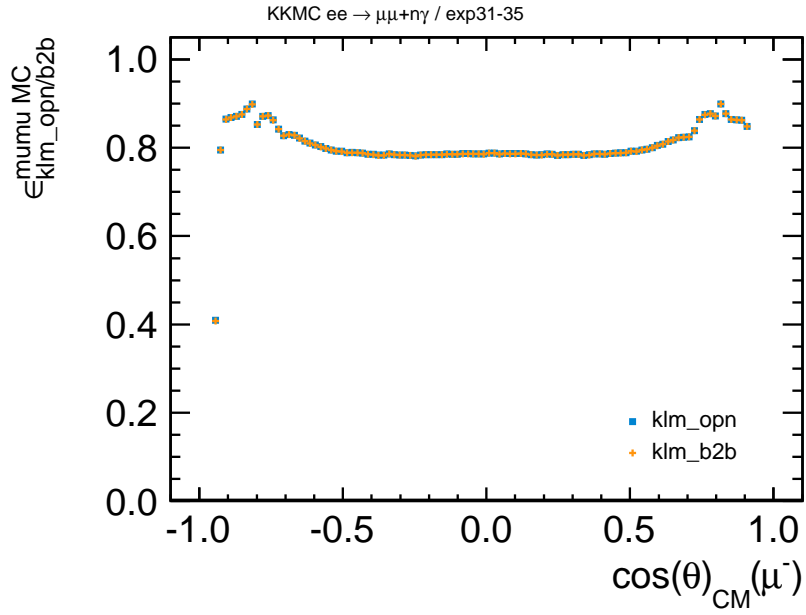
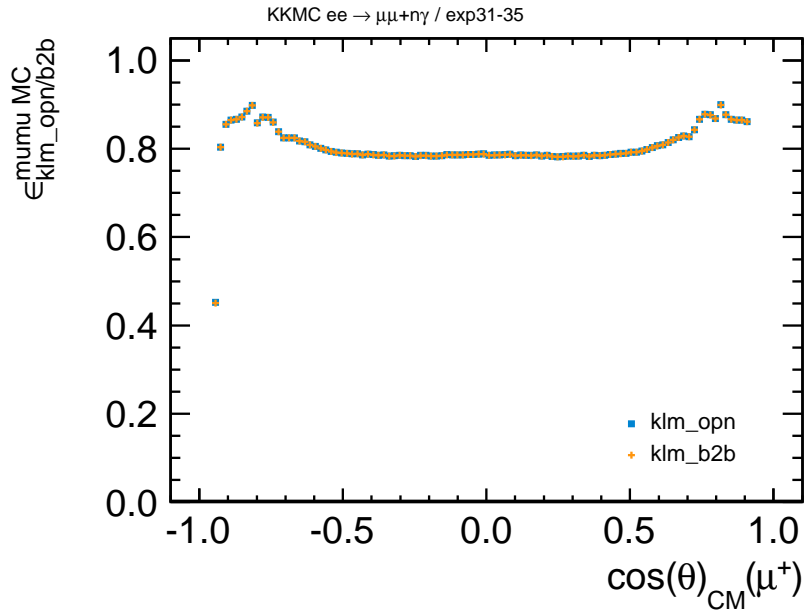


Figure 4.13:  $\cos(\theta)_{\text{Lab}}$  distribution of  $\epsilon_{\text{klm\_opn}}^{\text{mumu MC}}$  (PSV=1) and  $\epsilon_{\text{klm\_b2b}}^{\text{mumu MC}}$  (PSV=1) for  $\mu^+$ .



**Figure 4.14:**  $\cos(\theta)_{CM}$  distribution of  $\epsilon_{klm\_opn}^{mumu MC}$  (PSV=1) and  $\epsilon_{klm\_b2b}^{mumu MC}$  (PSV=1) for  $\mu^-$ .



**Figure 4.15:**  $\cos(\theta)_{CM}$  distribution of  $\epsilon_{klm\_opn}^{mumu MC}$  (PSV=1) and  $\epsilon_{klm\_b2b}^{mumu MC}$  (PSV=1) for  $\mu^+$ .

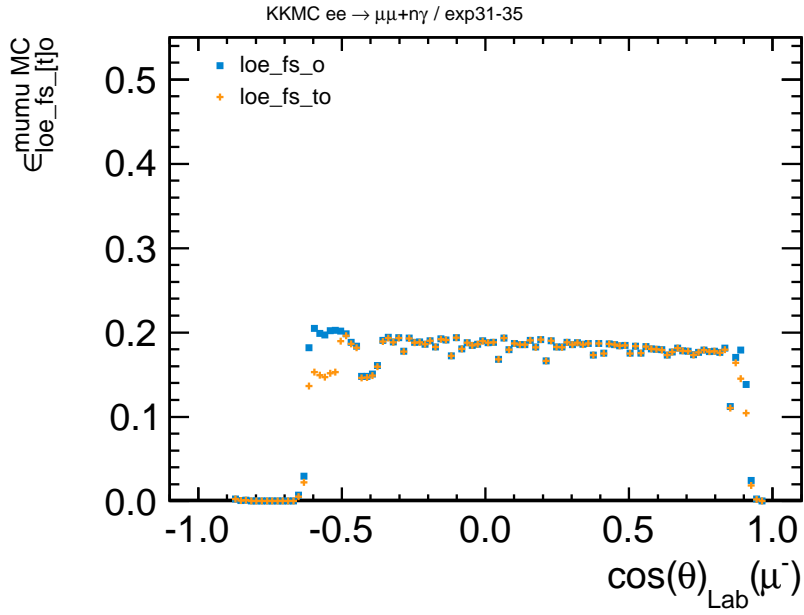


Figure 4.16:  $\cos(\theta)_{\text{Lab}}$  distribution of  $\epsilon_{\text{loe\_fs\_o}}^{\text{mumu MC}}$  (PSV=1) and  $\epsilon_{\text{loe\_fs\_to}}^{\text{mumu MC}}$  (PSV=1) for  $\mu^-$ .

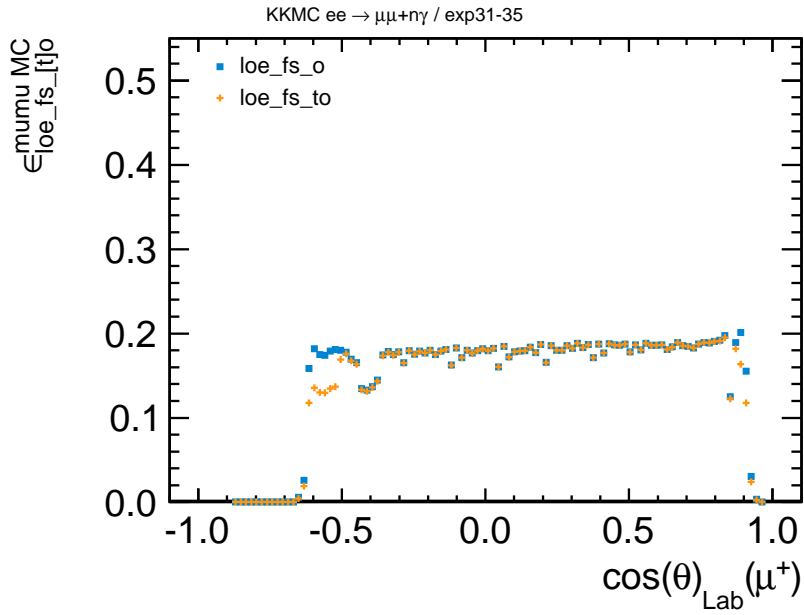
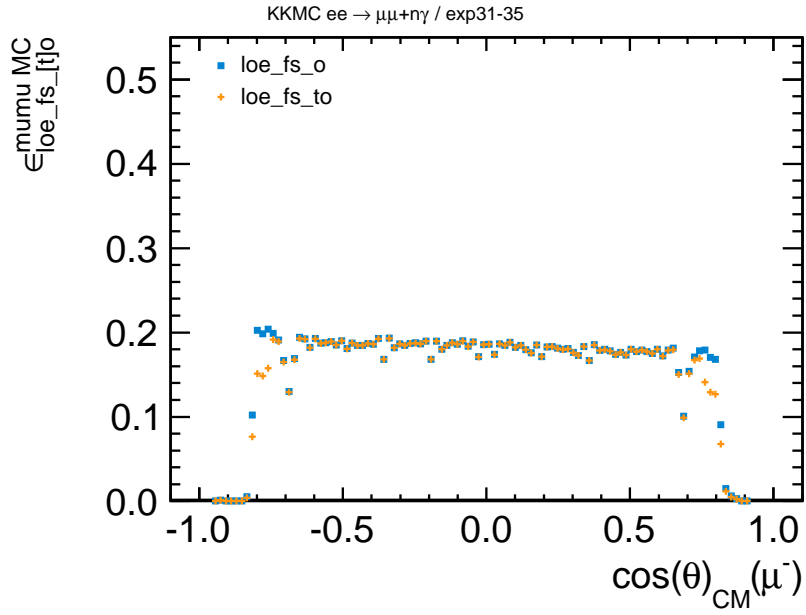
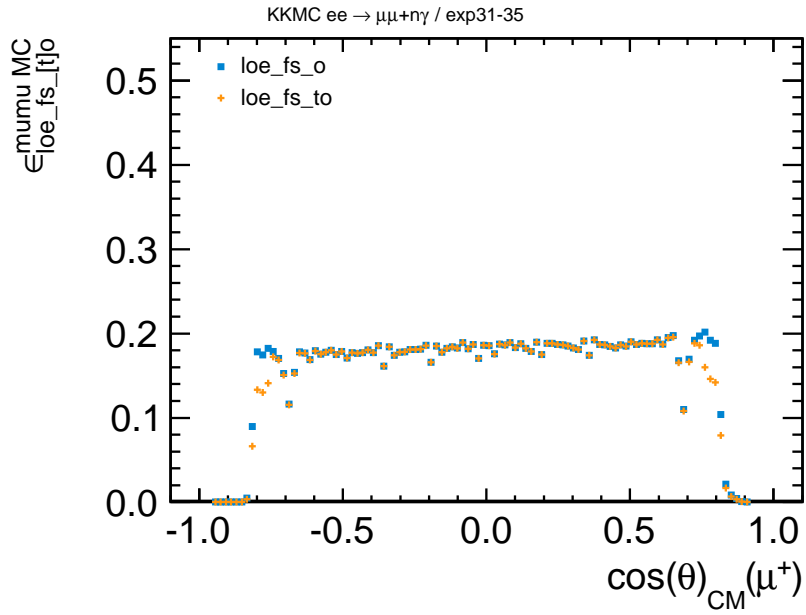


Figure 4.17:  $\cos(\theta)_{\text{Lab}}$  distribution of  $\epsilon_{\text{loe\_fs\_o}}^{\text{mumu MC}}$  (PSV=1) and  $\epsilon_{\text{loe\_fs\_to}}^{\text{mumu MC}}$  (PSV=1) for  $\mu^+$ .



**Figure 4.18:**  $\cos(\theta)_{CM}$  distribution of  $\epsilon_{loe\_fs\_ilo}^{mumu\ MC}$  (PSV=1) and  $\epsilon_{loe\_fs\_ito}^{mumu\ MC}$  (PSV=1) for  $\mu^-$ .



**Figure 4.19:**  $\cos(\theta)_{CM}$  distribution of  $\epsilon_{loe\_fs\_ilo}^{mumu\ MC}$  (PSV=1) and  $\epsilon_{loe\_fs\_ito}^{mumu\ MC}$  (PSV=1) for  $\mu^+$ .

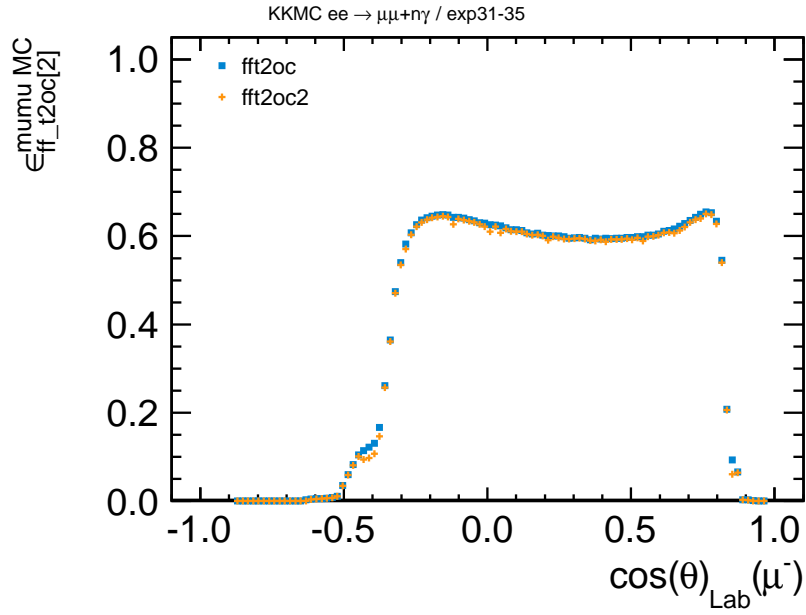


Figure 4.20:  $\cos(\theta)_{\text{Lab}}$  distribution of  $\epsilon_{\text{ff}_t2\text{oc}}^{\text{mumu MC}}$  (PSV=1) and  $\epsilon_{\text{ff}_t2\text{oc}2}^{\text{mumu MC}}$  (PSV=1) for  $\mu^-$ .

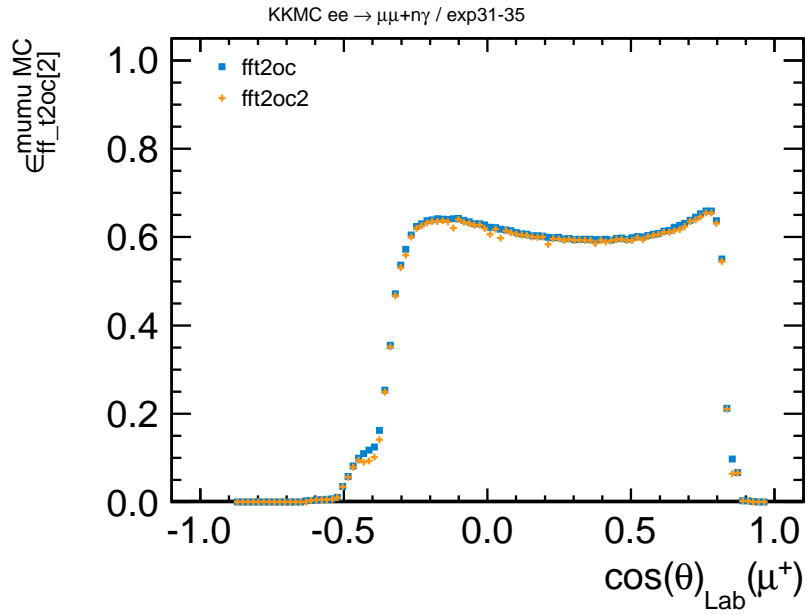
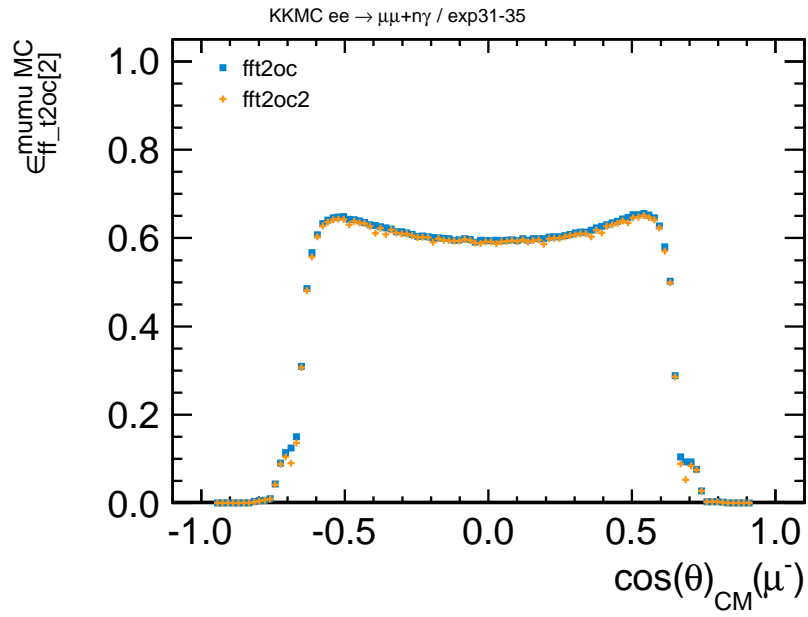
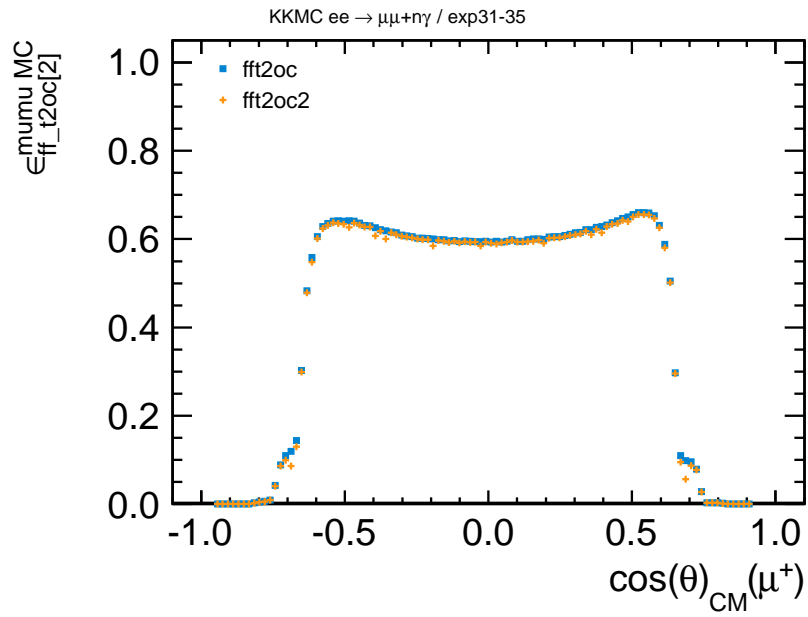


Figure 4.21:  $\cos(\theta)_{\text{Lab}}$  distribution of  $\epsilon_{\text{ff}_t2\text{oc}}^{\text{mumu MC}}$  (PSV=1) and  $\epsilon_{\text{ff}_t2\text{oc}2}^{\text{mumu MC}}$  (PSV=1) for  $\mu^+$ .



**Figure 4.22:**  $\cos(\theta)_{\text{CM}}$  distribution of  $\epsilon_{\text{ff\_t2oc}}^{\text{mumu MC}}(\text{PSV}=1)$  and  $\epsilon_{\text{ff\_t2oc2}}^{\text{mumu MC}}(\text{PSV}=1)$  for  $\mu^-$ .



**Figure 4.23:**  $\cos(\theta)_{\text{CM}}$  distribution of  $\epsilon_{\text{ff\_t2oc}}^{\text{mumu MC}}(\text{PSV}=1)$  and  $\epsilon_{\text{ff\_t2oc2}}^{\text{mumu MC}}(\text{PSV}=1)$  for  $\mu^+$ .

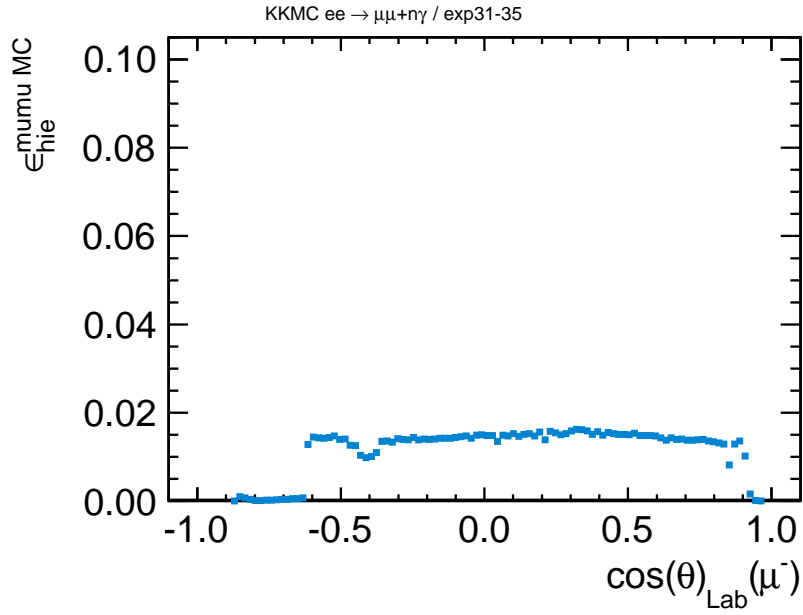


Figure 4.24:  $\cos(\theta)_{\text{Lab}}$  distribution of  $\epsilon_{\text{hie}}^{\text{mumu MC}}$  (PSV=1) for  $\mu^-$ .

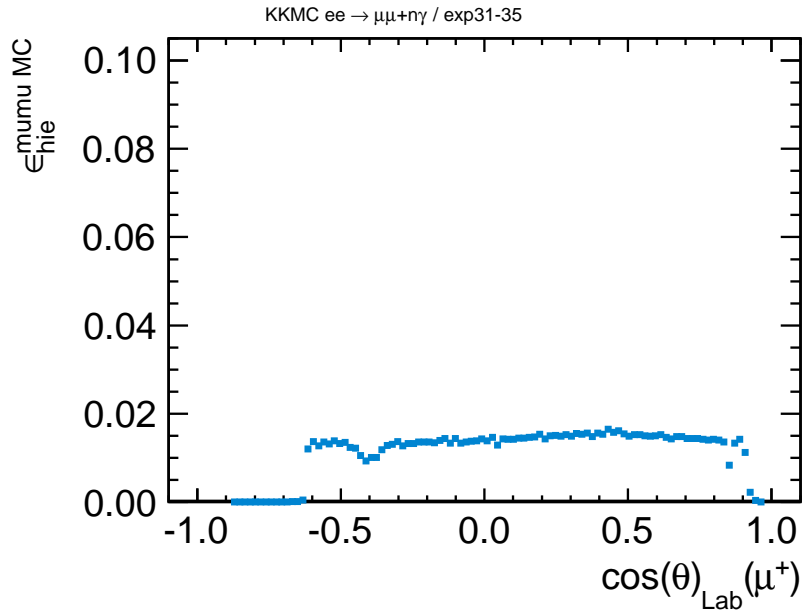


Figure 4.25:  $\cos(\theta)_{\text{Lab}}$  distribution of  $\epsilon_{\text{hie}}^{\text{mumu MC}}$  (PSV=1) for  $\mu^+$ .

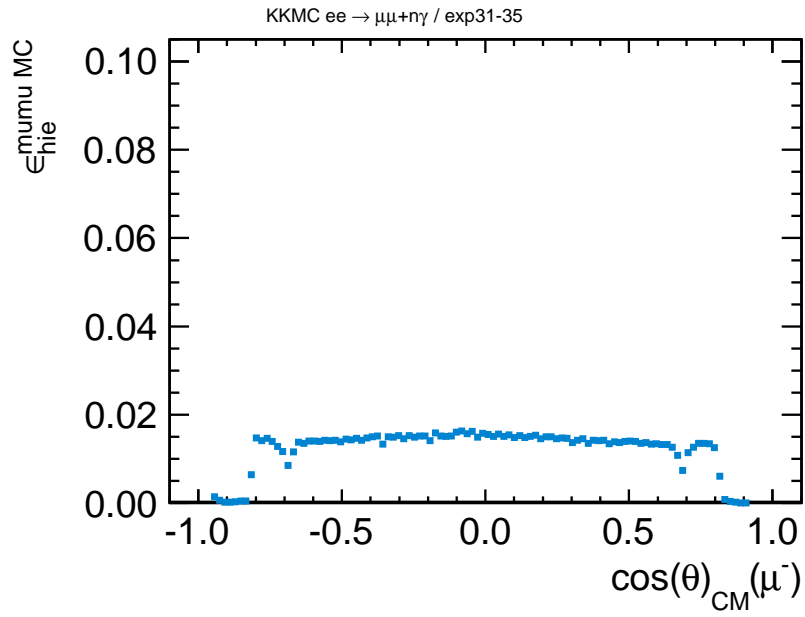


Figure 4.26:  $\cos(\theta)_{CM}$  distribution of  $\epsilon_{hie}^{mumu MC}$  (PSV=1) for  $\mu^-$ .

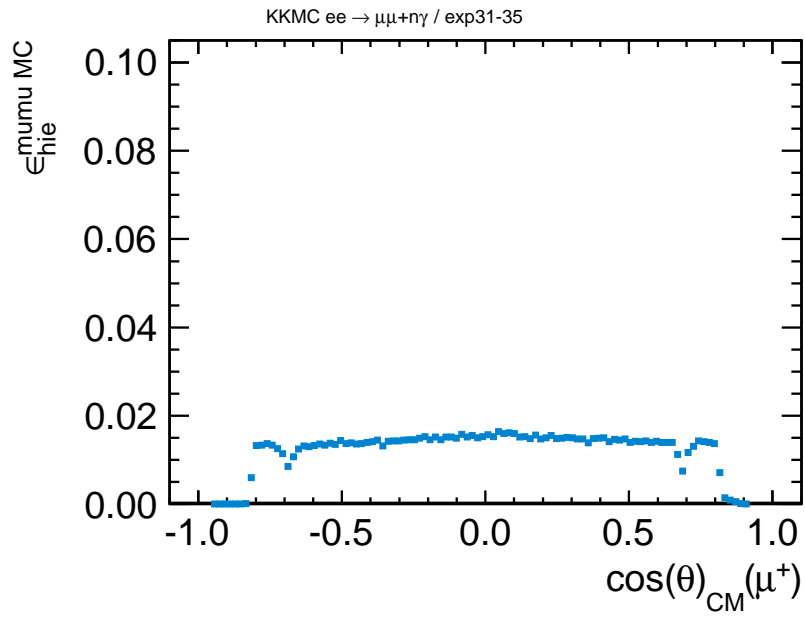


Figure 4.27:  $\cos(\theta)_{CM}$  distribution of  $\epsilon_{hie}^{mumu MC}$  (PSV=1) for  $\mu^+$ .

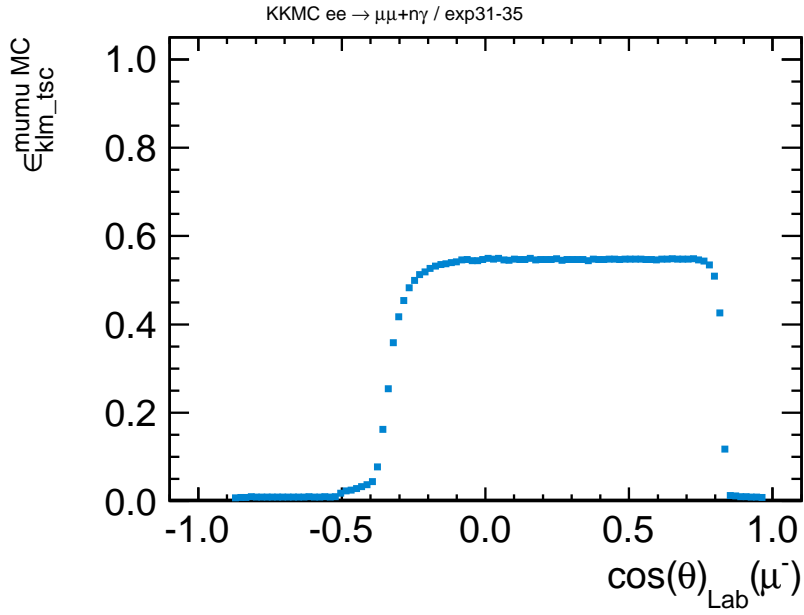


Figure 4.28:  $\cos(\theta)_{Lab}$  distribution of  $\epsilon_{klm\_tsc}^{mumu MC}$  (PSV=10) for  $\mu^-$ .

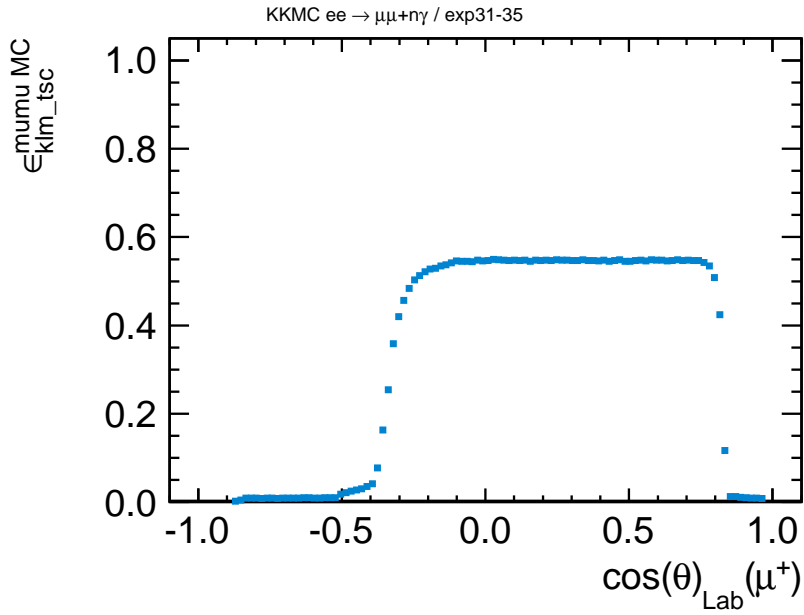


Figure 4.29:  $\cos(\theta)_{Lab}$  distribution of  $\epsilon_{klm\_tsc}^{mumu MC}$  (PSV=10) for  $\mu^+$ .

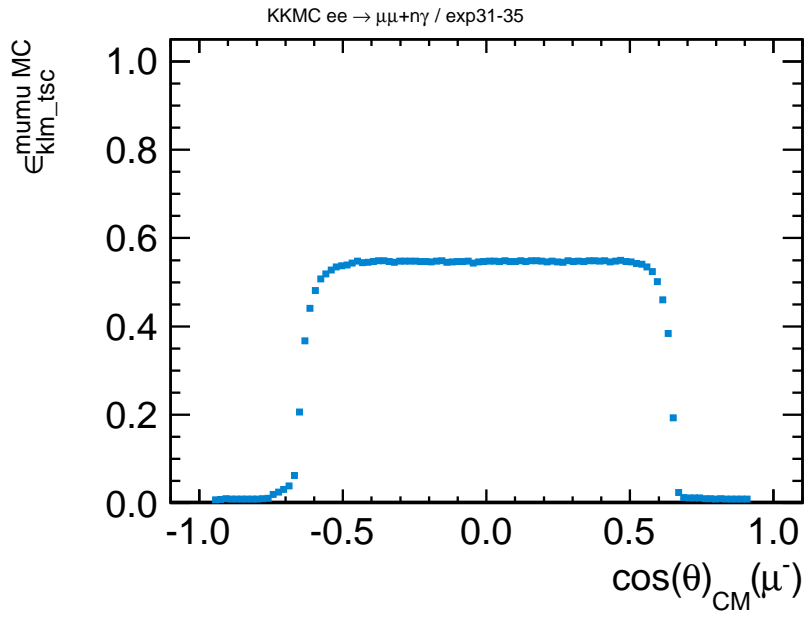


Figure 4.30:  $\cos(\theta)_{CM}$  distribution of  $\epsilon_{klm\_tsc}^{mumu MC}$  (PSV=10) for  $\mu^-$ .

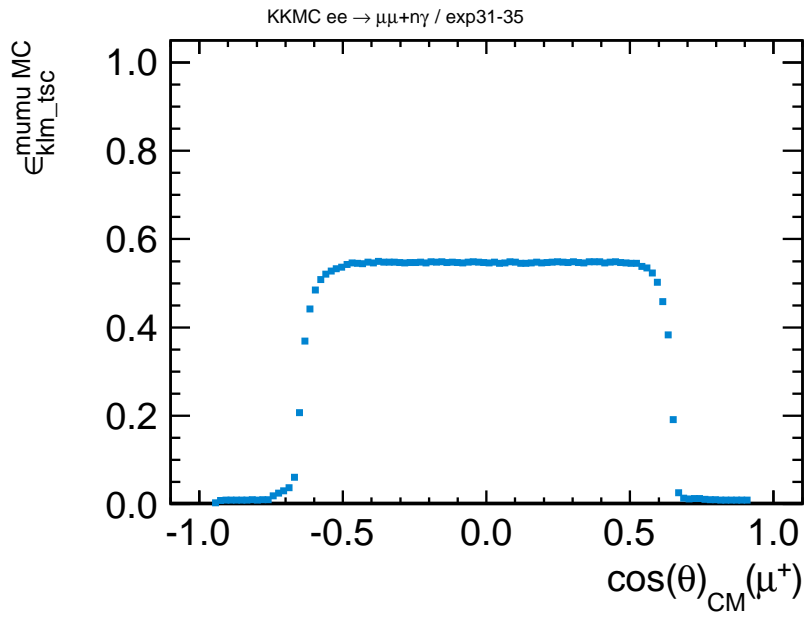
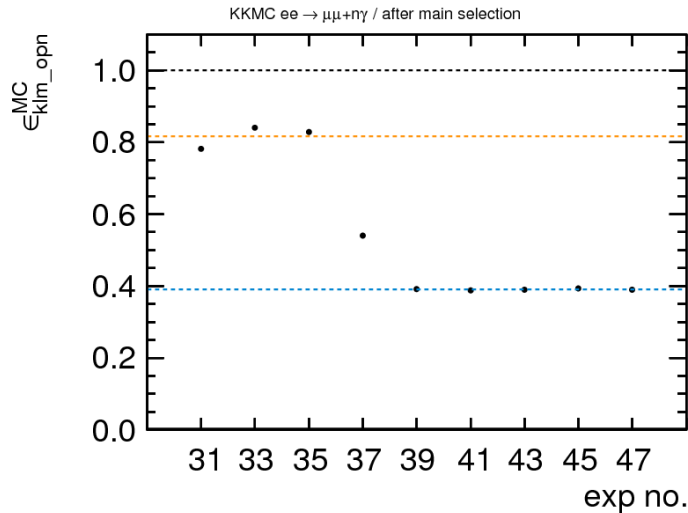


Figure 4.31:  $\cos(\theta)_{CM}$  distribution of  $\epsilon_{klm\_tsc}^{mumu MC}$  (PSV=10) for  $\mu^+$ .

### The CDC Trigger Issue

When checking  $\epsilon_{\text{klm\_opn}}^{\text{mumu MC}}$  for various experiments, a remarkable efficiency drop was noted between exp35 and exp39, which can be seen in Figure 4.32. The efficiency is about 82% for exp31 to exp35, about 54% for exp37 and only about 39% for exp39 and subsequent experiments, which is a much smaller value than expected. Figure 4.33 shows  $\epsilon_{\text{klm\_opn}}^{\text{mumu MC}}$  for a number of single runs within exp37. Here, the efficiency jumps between high and low values, which is an unusual and unphysical behaviour.

Further tests pointed out that all tested (sub)triggers using CDC information show a similar behaviour like the klm\_opn trigger bit, whereas all tested CDC-independent (sub)triggers have relatively constant efficiencies. Evidence for changes in the (sub)trigger definitions were not found. Since no comparable behaviour is visible neither in eemm and tautau MCs, nor in real data<sup>1</sup>, the conclusion was drawn that the cause must be a problem during trigger simulation for the mumu MCs. Since not all necessary information is available, it is not possible to re-run the trigger simulations only. Therefore, only exp31 to exp35 can be used for the determination of the L1 trigger efficiency determination within this thesis.



**Figure 4.32:** Efficiency of klm\_opn trigger for exp31 to exp47 with respect to all selected events. The orange (blue) line indicates the mean of the first three (last five) data points.

<sup>1</sup>For real data, orthogonal triggers were used for the trigger efficiency checks. See chapter 4.3.2. for an explanation.

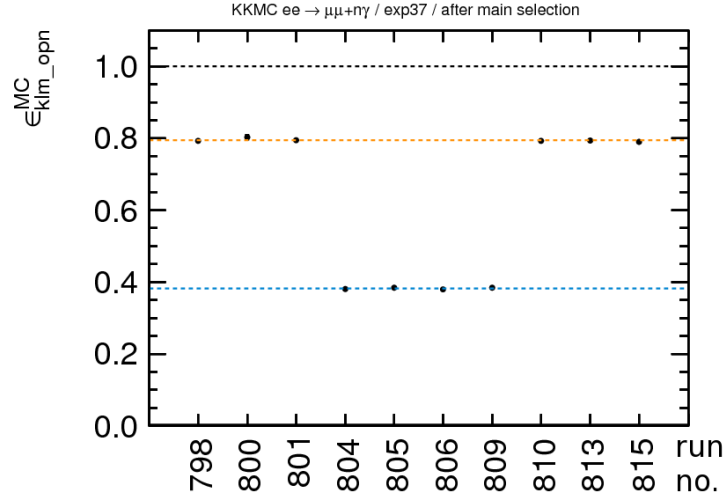


**Figure 4.33:** Efficiency of klm\_opn trigger for ten runs from exp37 with respect to all selected events. The orange (blue) line indicates the mean of the six upper (four lower) data points.

### 4.3.2 Trigger Efficiency from Orthogonal Triggers

When working with real data instead of MC, a different approach must be used, because the total number of events (including untriggered events) is unknown. There are several ways to determine trigger efficiencies from real data, for example the *Tag & Probe* method, which is generally well suited for dilepton events. Within this method, a *tag* with very tight selection criteria and very low fake rate, a *probe* with looser criteria and a *passing probe* are defined. The *passing probe* lepton usually has tighter criteria than the *probe*, but not tighter than the *tag*. In general, the efficiency of the *probe* is then the number of *passing probes* divided by the total number of *probes*. However, this method is better suited for determining single track trigger efficiencies and cannot be applied in this case.

Another method is the so-called *Bootstrapping* method, in which a less restrictive trigger (for example a low energy trigger) is used to determine the efficiency of a more restrictive trigger (for example a high energy trigger). This method is not ideal for the given trigger scenario either.

The most promising approach is the *Orthogonal Trigger* method. Therefore, at least two ideally independent triggers are needed. For example, energy triggers can be used to create an unbiased sample in order to test a muon trigger.

When considering two trigger bits A and B, their trigger efficiencies can be defined as:

$$\epsilon_{(\text{orth}) A} = \frac{A \& B}{B} \quad \text{and} \quad \epsilon_{(\text{orth}) B} = \frac{A \& B}{A}. \quad (4.7)$$

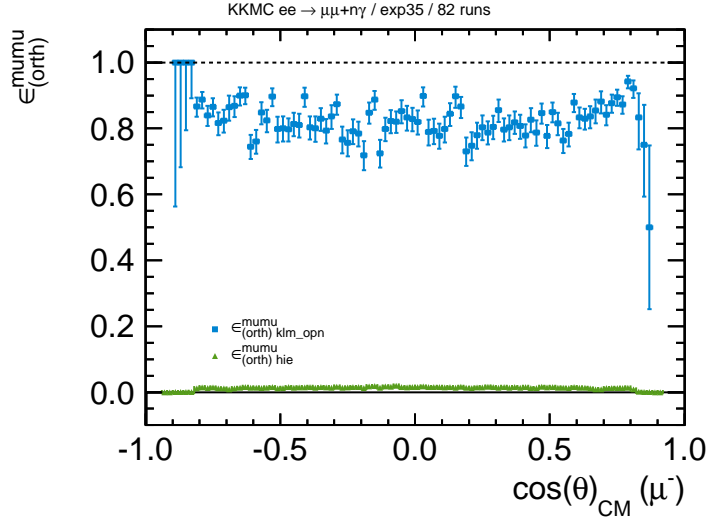


**Figure 4.34:** Trigger efficiencies  $\epsilon_{(orth)}^{mumu} \text{ klm\_opn}$  and  $\epsilon_{(orth)}^{mumu} \text{ hie}$  for selected events from exp35 (82 runs).

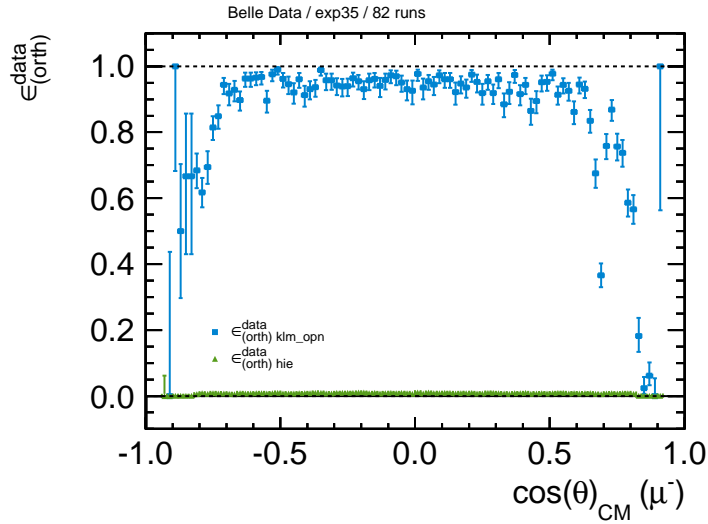


**Figure 4.35:** Trigger efficiencies  $\epsilon_{(orth)}^{data} \text{ klm\_opn}$  and  $\epsilon_{(orth)}^{data} \text{ hie}$  for selected events from exp35 (82 runs).

The only triggers bits truly independent from all others are the random triggers. Though trigger bits made up of different subtriggers can also be viewed as nearly independent, for example `klm_opn` (using CDC and KLM information only) and `hie` (using ECL information only). These trigger bits were used to calculate the efficiencies  $\epsilon_{(\text{orth}) \text{ klm\_opn}}$  and  $\epsilon_{(\text{orth}) \text{ hie}}$  according to Equation 4.7 both for the signal MC (Figure 4.34) and for experimental data (Figure 4.35). For this purpose, only runs from `exp35`, which were available for both MC and data at this point, were used. They amount to a total luminosity of  $1611 \text{ pb}^{-1}$  (82 runs).

In the central region is about  $(95.6 \pm 0.3) \%$ , whereas towards the two endcaps it decreases rapidly. In general,  $\epsilon_{(\text{orth}) \text{ klm\_opn}}^{\text{data}}$  and  $\epsilon_{(\text{orth}) \text{ klm\_opn}}^{\text{mumu}}$  should be the same, but as the MC precision is limited and systematical uncertainties are unavoidable to a certain extent, they are not expected to agree perfectly. The disagreement can be quantified, though, and used to correct the signal MC, such that it can be used for further analyses. Therefore, the ratio  $\epsilon_{(\text{orth}) \text{ klm\_opn}}^{\text{data}} / \epsilon_{(\text{orth}) \text{ klm\_opn}}^{\text{mumu}}$  ( $\cos(\theta)_{\text{CM}}$ ) is calculated, see Figure 4.36. In this case the disagreement between data and muon MC is rather large: In the central region, the `klm_opn` efficiency in data is about 15% higher than in the signal MC. Whereas towards the endcap regions, the ratio switches and shows higher `klm_opn` efficiencies in the signal MC than in experimental data. Although only a limited set of statistics was used, the statistical uncertainties of  $\epsilon_{(\text{orth}) \text{ klm\_opn}}^{\text{data}}$  and  $\epsilon_{(\text{orth}) \text{ klm\_opn}}^{\text{mumu}}$  are too small account for this huge difference. Apparently, the trigger simulation for the muon MC is not capable of precisely describing the actual `klm_opn` efficiency from the experiment. A possible reason is that the problem concerning all CDC-related subtriggers (presented in the previous subchapter) may not only affect `exp37` and following experiments, but possibly every experiment within the SVD2 set.

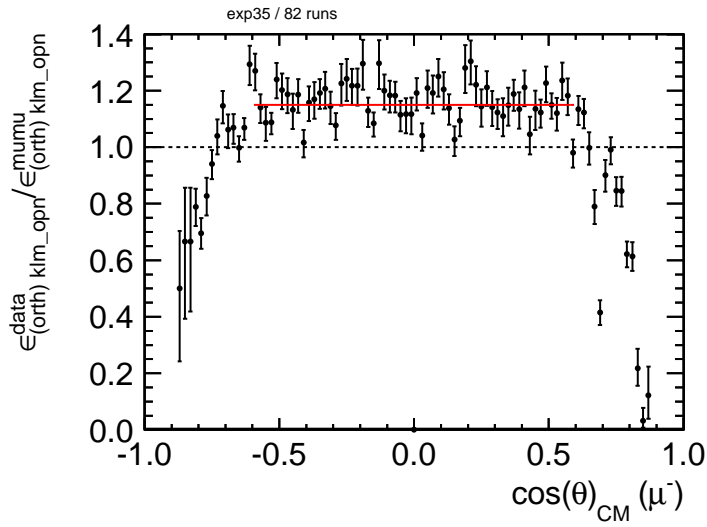


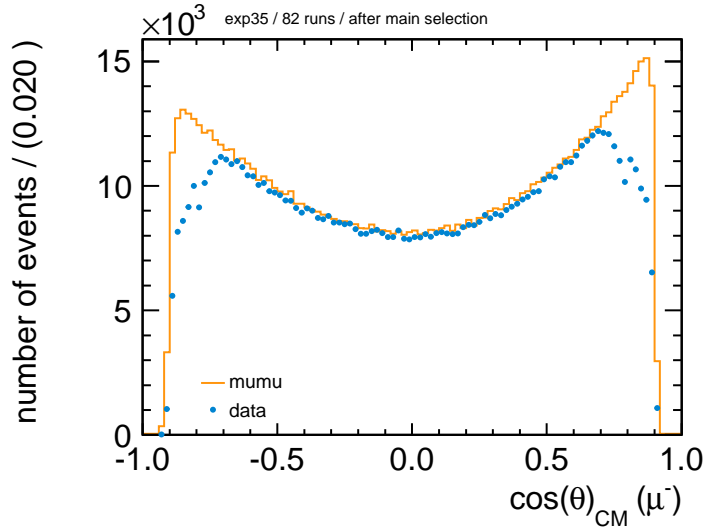
**Figure 4.36:** Ratio  $\epsilon_{(orth) klm\_opn}^{data} / \epsilon_{(orth) klm\_opn}^{mumu}$  for selected events from exp35 (82 runs). In the barrel region, where both trigger efficiencies and agreement between data and simulation were expected to be high, the ratio is  $1.149 \pm 0.008$  ( $\chi^2$  fit, red line).

Alternatively, the  $\cos(\theta)_{\text{CM}}$  distribution gained from MC can be corrected directly with the experimental `klm_opn` efficiency. In other words:  $\epsilon_{(\text{orth}) \text{klm\_opn}}^{\text{mumu}}$  is assumed to equal one, such that the ratio discussed above becomes equal to  $\epsilon_{(\text{orth}) \text{klm\_opn}}^{\text{data}}$ .

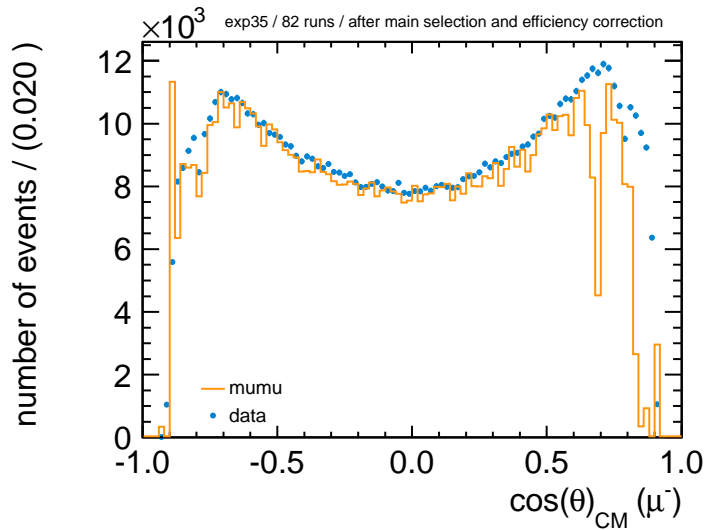
Figure 4.37 shows the angular distribution of all selected events for signal MC and experimental data. The first is shown without any trigger requirements (that means, triggered and untriggered events are included), whereas the latter automatically shows only events that were triggered. Applying all selection criteria introduced in the previous chapter, the two distributions already show quite good agreement in the barrel region. Background from `eemm` and `tautau` is negligible, as shown before, and is thus not included in this plot.

Figure 4.38 shows the same angular distributions like Figure 4.37 with  $\epsilon_{(\text{orth}) \text{klm\_opn}}^{\text{data}}$  applied on the signal MC distribution and only `klm_opn` triggered events in the data distribution. The low efficiency in the endcap regions corrects the number of signal MC events in that area down to match the data. The corrected signal MC histogram shows two bins (at  $\cos(\theta)_{\text{CM}} = \pm 0.91$ ) with seemingly too high bin content. This is due to low statistics which becomes obvious when comparing with Figure 4.35, which shows an efficiency of 100% at these points but with very high statistical uncertainties. The dip at  $\cos(\theta)_{\text{CM}} = 0.67 - 0.69$  (corresponding to one of the ECL gaps around 32 degrees in the laboratory frame) comes from an apparent surplus of `hie` triggered events. Checks with other orthogonal triggers – like a random trigger – are crucial here to understand this behaviour.

Figure 4.39 shows the ratio of all selected, `klm_opn` triggered events from experimental data and all selected events from the signal MC after the `klm_opn` efficiency correction. In the barrel region, the two distributions agree within a range of about 1.6%. By repeating this analysis step with higher statistics and additionally with different orthogonal triggers and by taking into account all systematical uncertainties, it should be possible to achieve an even better agreement.



**Figure 4.37:**  $\cos(\theta)_{\text{CM}}(\mu^-)$  for both signal MC and experimental data for selected events from exp35 (82 runs). Statistical uncertainties are in the order of  $10^2$  and are therefore not visible in this plot.



**Figure 4.38:**  $\cos(\theta)_{\text{CM}}(\mu^-)$  for both signal MC and experimental data for selected events from exp35 (82 runs) after the `klm_opn` efficiency correction on the signal MC. Only experimental data triggered by the `klm_opn` trigger is shown. Statistical uncertainties are in the order of  $10^2$  and are therefore not visible in this plot.

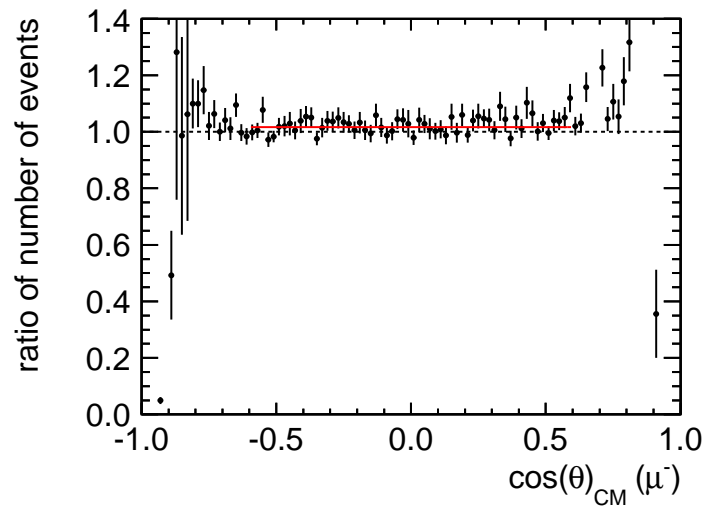


**Figure 4.39:** Ratio of the two angular distributions in Figure 4.38:  $\cos(\theta)^{\text{data}}/\cos(\theta)_{\text{CM}}^{\text{mumu}}$ . In the barrel region, the ratio is  $1.016 \pm 0.004$  ( $\chi^2$  fit, red line).

## Chapter 5

# Conclusion

A MC based event selection for picking  $e^+e^- \rightarrow \mu^+\mu^-$  events was developed, yielding an efficiency of  $\epsilon_{\text{selection}}^{\text{mumu exp35}} = (53.19 \pm 0.02)\%$  with respect to all MC generated  $e^+e^- \rightarrow \mu^+\mu^- + n\gamma$  events. This event selection reduces backgrounds from radiative Bhabha, radiative tau pairs, two-photon muon pair production, light quark pairs, charm quark pairs,  $\Upsilon(4S) \rightarrow B^0\bar{B}^0$  and  $\Upsilon(4S) \rightarrow B^+B^-$  to a negligible level with muons from two-photon muon pair production ( $e^+e^- \rightarrow e^+e^-\mu^+\mu^-$ ) being the largest remaining background. Backgrounds from radiative return pion pair production and cosmic muons are expected to be small but should be included in further analysis. For runs at lower mass resonances  $\Upsilon(1/2/3S)$ , the direct decays of these into muon pairs have to be included.

Using the Belle trigger simulation, suitable track and calorimeter based triggers for the  $A_{\text{FB}}$  analysis were found. It was discovered that the trigger simulation for the muon pair MC clearly shows faulty behaviour for CDC related (sub)trigger bits in Experiment 37 and following experiments. The conclusion was drawn, that only Experiment 31, Experiment 33 and Experiment 35 can be used for further MC based trigger investigations. This problem was not found in other MC samples like tau pair or two-photon muon pair production. The trigger efficiency for the most important CDC and KLM based trigger `k1m_opn` has been determined from data and the muon pair MC trigger simulation as a function of the polar angle  $\cos(\theta_{\text{CM}})$ , using `hie` as an orthogonal trigger. In the experiment, the `k1m_opn` trigger shows very high efficiency of about 95.6% in the barrel region and decreasing efficiencies towards both endcap regions, as expected beforehand. The efficiency determined from the trigger simulation truth information is in strong disagreement with the efficiency obtained from data such that it is not advisable to rely on the trigger simulation for muon pair MC for further analyses. The muon pair MC can be corrected directly with trigger efficiencies determined from data.

Knowing and understanding the angular shape of the trigger efficiency is very important because it directly influences the analysis of the forward-backward asymmetry. Therefore, the trigger study must be carried on. First of all, other trigger bit combinations should be taken into consideration, for example random

triggers. This should be possible when using higher statistics. Another interesting trigger bit may be the `klm_tsc` trigger, which is not completely orthogonal to the `klm_opn` trigger because they both depend on the KLM, but it requires a certain TOF hit pattern leading to a very flat efficiency in the central region (see e.g. Figure 4.30). Apart from that, the next steps should include an examination of the L3 and L4 trigger efficiencies, which were up to this point assumed to be 100%. Due to the event topology and kinematics, this is a justifiable assumption. Yet, this should be looked into in more detail. Furthermore, asymmetries of the detector itself and differences in the detection of  $\mu^+$  and  $\mu^-$  must be investigated.

While Belle is expected to be limited by statistics, the data that will be available at Belle II should allow a measurement of the Weinberg angle with similar statistical accuracy as at LEP/SLAC. Therefore, the planned Belle II trigger system upgrade using more (partial) orthogonal track based triggers to keep trigger related systematic uncertainties under control seems crucial for this analysis.

# Appendix A

## The Fast Track Finder Fzisan

*Fzisan* uses CDC data to find hit clusters. Clusters with more than two hits in  $\phi$  direction are discarded at once. The rest can be classified as *clean segments*, *short segments* or *complicated segments*, as indicated in Figure A.1. The complicated ones are discarded as well, whereas short segments are connected with each other or with single hits, if possible, to make them longer. After that, the segments are linked to 2D ( $r-\phi$ ) track candidates in an iterative process, as indicated in Figure A.2. The  $r-\phi$  track fitting is then completed after a three-step fit removing false hits and tracks, applying an event timing correction, solving the left-right track bending ambiguity, and determining the three track parameters  $dr$ ,  $\kappa$  (inverse of signed  $p_t$ ) and  $\phi_0$ . The stereo segments are linked afterwards in a rather similar procedure ( $s-z$  track fitting), such that 3D tracks can be built and two more track parameters ( $dz$  and  $P_z/P_t = \tan \lambda$ ) are obtained [30].

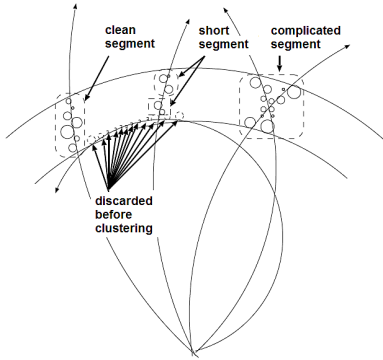


**Figure A.1:** Scheme of the hit clustering process during 2D track building within the L4 trigger. Adapted from [30].

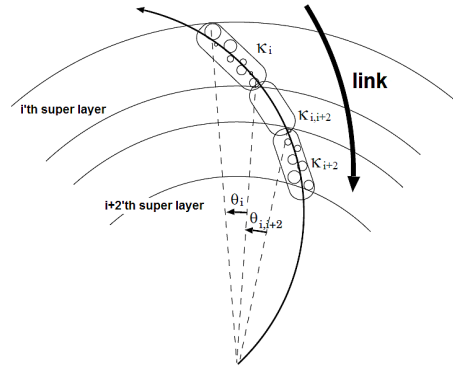


**Figure A.2:** Scheme of the segment linking process during 2D track building within the L4 trigger. Adapted from [30].

# List of Tables

4.1	Selection efficiencies for signal and background MCs . . . . .	24
4.2	Overview of all applied selection criteria . . . . .	27
4.3	Total selection efficiencies for signal and background MCs . . . . .	29
4.4	$\epsilon_{L1\text{ trg }i}^{\text{MC}}$ (single and combinatory) . . . . .	31

# List of Figures

2.1	Elementary Particle Interactions . . . . .	2
2.2	$\sin^2\theta_{W(\text{eff})}(Q)$ (theory and measurements) . . . . .	5
3.1	Schematic drawing of KEKB . . . . .	9
3.2	Integrated luminosity of KEKB and PEP II . . . . .	9
3.3	The Belle Detector . . . . .	10
3.4	Angular KLM efficiency . . . . .	11
3.5	The Belle Trigger System . . . . .	12
3.6	Data flow within the L4 trigger . . . . .	14
3.7	Scheme of the offline data flow . . . . .	15
4.1	$E_{\gamma \text{max}}$ distribution of preselected events . . . . .	20
4.2	Selection efficiency and purity for different $E_{\gamma \text{max}}$ cuts . . . . .	21
4.3	$\text{collin}_{\text{CM}}$ distribution of preselected events . . . . .	22
4.4	Selection efficiency $\epsilon_{\text{sel}}$ for different $\text{collin}_{\text{CM}}$ cuts . . . . .	22
4.5	$m_{\text{inv}}$ distribution of preselected events . . . . .	23
4.6	Selection efficiency $\epsilon_{\text{sel}}$ for different $m_{\text{inv}}$ cuts . . . . .	23
4.7	muID and eID distributions after main selection 1 (mumu) . . . . .	25
4.8	muID and eID distributions after main selection 1 (Bhabha) . . . . .	26
4.9	$\frac{E_{ECL}}{ p _{\text{Lab}}}$ distribution after main selection 1 (mumu and Bhabha) . . . . .	27
4.10	Number of events before $\frac{E_{ECL}}{ p _{\text{Lab}}}$ cuts . . . . .	28
4.11	Number of events after $\frac{E_{ECL}}{ p _{\text{Lab}}}$ cuts . . . . .	28
4.12	$\cos(\theta)_{\text{Lab}}$ distribution of $\epsilon_{\text{klm\_opn}/\text{b2b}}^{\text{mumu MC}}$ for $\mu^-$ . . . . .	33
4.13	$\cos(\theta)_{\text{Lab}}$ distribution of $\epsilon_{\text{klm\_opn}/\text{b2b}}^{\text{mumu MC}}$ for $\mu^+$ . . . . .	33
4.14	$\cos(\theta)_{\text{CM}}$ distribution of $\epsilon_{\text{klm\_opn}/\text{b2b}}^{\text{mumu MC}}$ for $\mu^-$ . . . . .	34
4.15	$\cos(\theta)_{\text{CM}}$ distribution of $\epsilon_{\text{klm\_opn}/\text{b2b}}^{\text{mumu MC}}$ for $\mu^+$ . . . . .	34
4.16	$\cos(\theta)_{\text{Lab}}$ distribution of $\epsilon_{\text{loe\_fs\_}[t]o}^{\text{mumu MC}}$ for $\mu^-$ . . . . .	35
4.17	$\cos(\theta)_{\text{Lab}}$ distribution of $\epsilon_{\text{loe\_fs\_}[t]o}^{\text{mumu MC}}$ for $\mu^+$ . . . . .	35
4.18	$\cos(\theta)_{\text{CM}}$ distribution of $\epsilon_{\text{loe\_fs\_}[t]o}^{\text{mumu MC}}$ for $\mu^-$ . . . . .	36
4.19	$\cos(\theta)_{\text{CM}}$ distribution of $\epsilon_{\text{loe\_fs\_}[t]o}^{\text{mumu MC}}$ for $\mu^+$ . . . . .	36
4.20	$\cos(\theta)_{\text{Lab}}$ distribution of $\epsilon_{\text{ff\_t2oc}[2]}^{\text{mumu MC}}$ for $\mu^-$ . . . . .	37
4.21	$\cos(\theta)_{\text{Lab}}$ distribution of $\epsilon_{\text{ff\_t2oc}[2]}^{\text{mumu MC}}$ for $\mu^+$ . . . . .	37
4.22	$\cos(\theta)_{\text{CM}}$ distribution of $\epsilon_{\text{ff\_t2oc}[2]}^{\text{mumu MC}}$ for $\mu^-$ . . . . .	38

4.23	$\cos(\theta)_{\text{CM}}$ distribution of $\epsilon_{\text{ff.t2oc}[2]}^{\text{mumu MC}}$ for $\mu^+$	38
4.24	$\cos(\theta)_{\text{Lab}}$ distribution of $\epsilon_{\text{hie}}^{\text{mumu MC}}$ for $\mu^-$	39
4.25	$\cos(\theta)_{\text{Lab}}$ distribution of $\epsilon_{\text{hie}}^{\text{mumu MC}}$ for $\mu^+$	39
4.26	$\cos(\theta)_{\text{CM}}$ distribution of $\epsilon_{\text{hie}}^{\text{mumu MC}}$ for $\mu^-$	40
4.27	$\cos(\theta)_{\text{CM}}$ distribution of $\epsilon_{\text{hie}}^{\text{mumu MC}}$ for $\mu^+$	40
4.28	$\cos(\theta)_{\text{Lab}}$ distribution of $\epsilon_{\text{klm.tsc}}^{\text{mumu MC}}$ for $\mu^-$	41
4.29	$\cos(\theta)_{\text{Lab}}$ distribution of $\epsilon_{\text{klm.tsc}}^{\text{mumu MC}}$ for $\mu^+$	41
4.30	$\cos(\theta)_{\text{CM}}$ distribution of $\epsilon_{\text{klm.tsc}}^{\text{mumu MC}}$ for $\mu^-$	42
4.31	$\cos(\theta)_{\text{CM}}$ distribution of $\epsilon_{\text{klm.tsc}}^{\text{mumu MC}}$ for $\mu^+$	42
4.32	$\epsilon_{\text{klm.opn}}^{\text{mumu MC}}$ for exp31 to exp47	43
4.33	$\epsilon_{\text{klm.opn}}^{\text{mumu MC}}$ for exp37, run798–815	44
4.34	Orthogonal trigger efficiencies for klm_opn and hie (mumu)	45
4.35	Orthogonal trigger efficiencies for klm_opn and hie (data)	45
4.36	Ratio $\epsilon^{\text{data}}/\epsilon_{\text{(orth) klm.opn}}^{\text{mumu}}$	47
4.37	$\cos(\theta)_{\text{CM}}(\mu^-)$ (mumu and data)	49
4.38	$\cos(\theta)_{\text{CM}}(\mu^-)$ (mumu and data) after trigger efficiency correction	49
4.39	Ratio $\cos(\theta)^{\text{data}}/\cos(\theta)_{\text{CM}}^{\text{mumu}}(\mu^-)$	50
A.1	Hit clustering process during L4 2D track building	53
A.2	Segment linking process during L4 2D track building	53

# Bibliography

- [1] P.W. Higgs. Broken symmetries and the masses of gauge bosons. 1964, Phys. Rev. Lett. 13, 508.
- [2] P.W. Higgs. Broken symmetries, massless particles and gauge fields. 1964, Phys. Rev. Lett. 12, 132.
- [3] F.Englert and R.Brout. Broken symmtry and the mass of gauge vector mesons. 1964, Phys. Rev. Lett. 13, 321.
- [4] [http://commons.wikimedia.org/wiki/File:Elementary\\_particle\\_interactions\\_new.svg](http://commons.wikimedia.org/wiki/File:Elementary_particle_interactions_new.svg). (Upload from February 2013).
- [5] S.L. Glashow. Partial symmetries of weak interactions. 1961, Nucl. Phys. 22, 579.
- [6] A. Salam. Weak and electromagnetic interactions. 1968, originally printed in: Svartholm: Elementary Particle Theory, Proceedings Of The Nobel Symposium held 1968 at Lerum, Sweden, Stockholm, 367-377.
- [7] S. Weinberg. A model of leptons. 1967, Phys. Rev. Lett. 19, 1264.
- [8] M. Gell-Mann. The interpretation of the new particles as displaced charge multiplets. 1956, Il Nuovo Cimento 4, Issue 2 Supplement, 848-866.
- [9] K. Nishijima. Charge Independence Theory of V Particles. 1955, Prog. Theor. Phys. 13 (3), 285-304.
- [10] J. Beringer et al. (Particle Data Group). 10. Electroweak model and constraints on new physics. 2012, Phys. Rev. D86, 010001.
- [11] The NuTeV Collaboration. A Precise determination of electroweak parameters in neutrino nucleon scattering. 2002, Phys.Rev.Lett. 88, 091802, arXiv:0110059.
- [12] Wood et al. Precision measurement of parity nonconservation in cesium. 1999, Can. J. Phys. 77, 775.
- [13] P.L. Anthony et al. Precision Measurement of the Weak Mixing Angle in Møller Scattering. 2005, arxiv:0504049v1.

- 
- [14] The ALEPH, DELPHI, L3, OPAL, SLD Collaborations, the LEP Electroweak Working Group, the SLD Electroweak and Heavy Flavour Groups. Precision Electroweak Measurements on the Z Resonance. 2006, Phys. Rept. 427, 257-454, arXiv:hep-ex/0509008v3.
- [15] The JADE Collaboration. Test of the Standard Model in Leptonic Reactions at PETRA Energies. 1986, Z. Phys. C, Particles and Fields 30, 371-380.
- [16] M. Goebel. Tests of the Electroweak Standard Model and Measurement of the Weak Mixing Angle with the ATLAS Detector. 2011, PhD thesis, University of Hamburg, Hamburg, Germany.
- [17] The CDF Collaboration. Measurement of the forward-backward charge asymmetry of electron positron pairs in  $p\bar{p}$  collisions at  $\sqrt{s} = 1.96$  TeV. 2005, Phys. Rev. D71, 052002, arXiv:0411059.
- [18] The CMS Collaboration. Forward-backward asymmetry of di-lepton pairs and the weak-mixing angle. 2011, CMS-PAS-EWK-10-011.
- [19] The D0 Collaboration. Measurement of  $\sin^2\theta_{\text{eff}}^{\text{lept}}$  and Z-light quark couplings using the forward-backward charge asymmetry in  $p\bar{p} \rightarrow Z/\gamma^* \rightarrow e^+e^-$  events with  $L = 5.0\text{fb}^{-1}$  at  $\sqrt{s} = 1.96$  TeV. 2011, arXiv:1104.4590.
- [20] T. Aushev et al. Physics at Super B Factory. 2010, KEK Report 2009-12, arXiv:1002.50128.
- [21] Jadach et al. The precision Monte Carlo event generator  $\mathcal{KK}$  for two-fermion final states in  $e^+e^-$  collisions. 2000, Comp. Phys. Comm. 130, 260-325.
- [22] [http://www-acc.kek.jp/kekb/commissioning/record/History\\_of\\_record.html](http://www-acc.kek.jp/kekb/commissioning/record/History_of_record.html). (Last accessed in 11.2013).
- [23] The BABAR Collaboration. The BABAR detector. 2002, Nucl. Instr. and Meth. in Physics Research A, 479, 1-116.
- [24] The BABAR Collaboration. The BABAR Physics Book: Physics at an Asymmetric B Factory. 1998, SLAC-R-504.
- [25] [http://belle.kek.jp/belle/slides/slide\\_index.html](http://belle.kek.jp/belle/slides/slide_index.html). (Last accessed in 11.2013).
- [26] [http://belle.kek.jp/bdocs/lumi\\_belle.png](http://belle.kek.jp/bdocs/lumi_belle.png). (Last accessed in 11.2013).
- [27] The Belle Collaboration. The Belle Detector. 2002, Nuclear Instruments and Methods in Physics Research A 479, 117232.
- [28] Piilonen et al. Belle Note 338: BELLE Muon Identification. 2000.
- [29] Ushiroda et al. Belle Preprint 99-1: Development of the Central Trigger System for the BELLE detector at the KEK B-factory. 1999.
- [30] Hanagaki et al. Belle Note 299: The Level 4 Software Trigger at BELLE. 2000.

- 
- [31] Nishida et al. Belle Note 680: Trigger Summary – experiment 31. 2004.
- [32] Ronga et al. New distributed offline processing scheme at Belle. 2004, arXiv:041200v1.
- [33] <http://belle.kek.jp/group/software/panther/>. (Last accessed in 11.2013).
- [34] R. Itoh. BASF - Belle Analysis Framework. 1997, Proceedings of the International Conference on Computing in High Energy Physics.
- [35] F.Berends, P.Daverveldt, R.Kleiss. Monte-Carlo simulation of two-photon processes. 1986, Comp. Phys. Comm. 40, 271-284, 285-307, 309-326.
- [36] G.Balossini, C.M.Carloni Calame, G.Montagna, O.Nicrosini, F.Piccinini. Matching perturbative and Parton Shower corrections to Bhabha process at flavour factories. 2006, Nucl. Phys. B758, 227-253, arXiv:0607181.
- [37] G.Balossini, C.Bignamini, C.M.Carloni Calame, G.Montagna, F.Piccinini, O.Nicrosini. Photon pair production at flavour factories with per mille accuracy. 2008, Phys. Lett. B663, 209-313, arXiv:0801.3360.
- [38] C.M.Carloni Calame, G.Montagna, O.Nicrosini, F.Piccinini. The babayaga event generator. 2004, Nucl. Phys. Proc. Suppl. 131, 48-55, arXiv:0312014.
- [39] C.M.Carloni Calame. An Improved Parton Shower algorithm in QED. 2001, Phys. Lett. B520, 16-24, arXiv:0103117.
- [40] C.M.Carloni Calame, C.Lunardini, G.Montagna, O.Nicrosini, F.Piccinini. Large-angle Bhabha scattering and luminosity at flavour factories. 2000, Nucl. Phys. B584, 459-479, arXiv:0003268.
- [41] Personal correspondence with T.Ferber, DESY. December 2012.
- [42] S. Banerjee et al. Tau and muon pair production cross sections in electron-positron annihilations at  $\sqrt{s} = 10.58$  GeV. 2008, arXiv:0706.3235v2.
- [43] J. Beringer et al. (Particle Data Group). Particle Listings. 2012, Phys. Rev. D86, 010001.

# Formal and Personal Issues

## Danksagung

Ich bedanke mich sehr herzlich bei Herrn Dr. Carsten Niebuhr für die Übertragung dieser interessanten Arbeit und seinen Einsatz als externer Zweitgutachter, sowie bei Frau Prof. Dr. Caren Hagner für ihren Einsatz als Erstgutachterin. Der gesamten Belle-Arbeitsgruppe am DESY in Hamburg spreche ich meinen Dank aus für die freundliche Aufnahme in die Gruppe sowie für wertvolles Feedback, zum Beispiel während meiner Vorbereitung auf die DPG-Tagung 2013 in Dresden, bei der ich einen Vortrag über mein Forschungsthema halten durfte. Ganz besonderer Dank gilt Herrn Dr. Torben Ferber, der diese Arbeit betreut hat. Seine geduldigen Erklärungen und zahlreichen Hilfestellungen weiß ich sehr zu schätzen, ebenso die vielen grauen Haare, die ich ihm im Laufe des vergangenen Jahres beschert habe – vielen, vielen Dank!

## Formelles

Hiermit bestätige ich, dass die vorliegende Arbeit von mir selbständig verfasst wurde und ich keine anderen als die angegebenen Hilfsmittel – insbesondere keine im Quellenverzeichnis nicht benannten Internet-Quellen – benutzt habe und die Arbeit von mir vorher nicht einem anderen Prüfungsverfahren eingereicht wurde. Die eingereichte schriftliche Fassung entspricht der auf dem elektronischen Speichermedium. Ich bin damit einverstanden, dass die Masterarbeit veröffentlicht wird.

Hamburg, 01.12.2013

---

(Kim Susan Petersen)